Enhancing organosilicon polymer-derived ceramic properties

Patricia A. Loughney,[1] Shakir B. Mujib,[2] Timothy L. Pruyn,[3] Gurpreet Singh,[2] Kathy Lu,[4] Vicky Doan-Nguyen[1,5]

[1] Department of Materials Science and Engineering, The Ohio State University, Columbus, Ohio 43212, USA
[2] Department of Mechanical and Nuclear Engineering, Kansas State University, Manhattan, Kansas 66507, USA.
[3] Air Force Research Laboratory, Wright-Patterson Air Force Base, Ohio, USA
[4] Department of Materials Science and Engineering, Virginia Polytechnic Institute and State University, Blacksburg, Virginia 24061, USA
[5] Department of Mechanical and Aerospace Engineering, The Ohio State University, Columbus, Ohio 43212, USA

Author to whom correspondence should be addressed: doan-nguyen.1@osu.edu
Electronic address: doan-nguyen.1@osu.edu

Keywords: Polymer-derived ceramics, electric conductivity, magnetism, energy conversion, energy storage, characterization

Abstract

Polymer derived ceramic (PDC) nanocomposites enable access to a large library of functional properties starting from molecular design as well as incorporating nanofillers. Tailoring preceramic polymer (PCP) chemistry and nanofiller size and morphology can lead to usage of the nanocomposites into complex shapes and coatings with enhanced thermal and mechanical properties. Rational design of targeted nanocomposites requires understanding of fundamental structure-property-performance relations. Thus, we tailor our discussions of PCP design and nanofiller integration into single source precursors as well as pyrolytic processing for functionalizing PDCs. We also discuss the promises and limitations of advanced characterization techniques such as 4D transmission electron microscopy and pair distribution functions to enable *in-situ* mapping structural evolution. The feedback loop of *in-situ* monitoring sets the foundation for enabling accelerated materials discovery with artificial intelligence. This perspective assesses

recent progress of PDC nanocomposite research nanocomposites and present scientific and engineering challenges for synthesis, fabrication, processing, and advanced characterization of PDC nanocomposites for enhanced magnetic, electrical, and energy conversion and storage properties.

1. Scope and content of perspective

Polymer derived ceramic (PDC) nanocomposites enable access to a large library of chemistries and functional properties. Tailoring preceramic polymer chemistry and nanofiller size and morphology can lead to usage of the nanocomposites into complex shapes and coatings with enhanced thermal and mechanical properties. This perspective will assess progress of the last 5 years of research on PDC nanocomposites and address open questions regarding fabrication and characterization of PDC nanocomposites for enhanced electrical, magnetic, and energy conversion and storage properties. This perspective is not intended to be an exhaustive review of the field; for this purpose, we point the reader to a selection of recent general reviews on PDCs[1–3] and investigations into modifying their microstructure[1,4–6] and mechanical properties[7] for coatings[4] and nanocomposite formulations[8,9].

Recently, the tailoring of polymer-derived composite included molecular modification of the polymer, incorporation of chemical additives,[10–12] incorporation of nanostructures,[13,14] grafting,[15,16] and microwave or plasma assisted pyrolysis,[17–20] to control microstructure, porosity, and mechanical properties that govern functionalities such as hydrophobicity, ultra-high temperature resistance, electrical conductivity, magnetism, charge storage, and catalysis. Additive manufacturing has also enabled form factors previously not accessible.[21,22]

Open questions remain for how functionalities are tuned and affected regarding the incorporation of nanofillers. In the case of electrical conductivity, it is anticipated that lower mass loading is needed to achieve percolative network with free carbon content in PDCs. Can preformed nanostructures be incorporated into polymer matrix with the size and shape distribution be maintained throughout pyrolysis? What is the influence of nanofillers and metal salt precursors on free carbon formation (onset temperature, nanostructures)? Concomitant with the incorporation of nanofillers to impart functional properties to PDCs, side chains and polymer backbone can be modified towards targeted applications. In the case of ultra-high temperature resistance, polycarbosilanes have been modified to chelate to Zn and Ti centers for producing metal carbide in SiC matrix composite from single source precursors.[23] Such composites with well-dispersed metal carbide nanoprecipitates have been demonstrated to be more temperature resistant with improved oxidation resistance. Such ultra-high temperature, oxidation, and erosion resistant properties enable usage in applications such as hypersonic vehicles or spacecraft in low Earth orbit (LEO). Materials-by-design require precise control of precursors, which can be achieved through synthesis of single source precursors.

Considering the above, the first part of this perspective will focus on molecular tuning of organosilicon precursors. The second part of this perspective will focus on inclusion of electrical, magnetic, and catalytic properties via nanofillers and metal salt additives to preceramic polymers. We aim to shed light on theoretical models to understand and design composites with enhanced percolative networks while reducing mass. The third part of this perspective will focus on enhancing electrochemical energy storage by using PDC electrodes. We present emerging techniques for electrode fabrication, such as additive manufacturing, that can control hierarchical porosity and intrinsic conductivity.

The final part of this perspective will lay out needs for advanced characterization for understanding structure-property-performance relations of functional PDCs. From high-temperature X-ray scattering to aberration-corrected scanning transmission electron microscopy, we summarize emerging techniques for cross-correlative *ex-situ* and *in-situ* characterization of PDC microstructural evolution.

2. Functionality from synthesis of preceramic polymers

Preceramic polymers are polymers and/or oligomers that contain both organic and inorganic molecular segments that thermally transform into an inorganic ceramic when subjected to high temperatures (i.e., pyrolysis). Often on the main atoms in preceramic polymers are Si, C, N, and O but other elements can be included into the polymer and evolve with the structure to introduce new properties and functionalities in the process. A generic structure can be seen in Fig. 1, in which Si is bonded to an element (E) that is often C (polycarbosilane), N (polysilazane), or O (polysiloxane). The functional groups off the Si (R_1 and R_2) are often hydrogen or organic moieties.[1–3] One of the advantages of producing ceramics from polymers is a broad palette of inorganic compositions. There are numerous binary systems that are derived from preceramic polymers such as SiO_2 and SiC composites,[24,25] silicon nitride (Si_3N_4),[26–28] and BN[29–34] but ternary and quaternary systems such as SiCN, SiCO, BCN, SiCNO, SiBCN, SiBCO, SiAlCN, and SiAlCO are also achievable.Click or tap here to enter text.[1–6,24] Significantly, many of these multicomponent ceramics possess improved thermal, chemical and mechanical properties and offer opportunities to incorporate functionality, relative to their binary parent systems. However, realizing such multicomponent ceramics poses synthetic challenges as each ceramic system or compositional changes has historically required the production of new preceramic polymers, involving the selection and optimization of reactions, reaction conditions, and product purification.

Silicon oxycarbide (SiOC) and silicon carbonitride (SiCN) are common ternary ceramic systems that have been heavily investigated and serve as the matrix in composites with excellent thermal, chemical, corrosion-resistant, and mechanical properties.[3,6,35–37] We will introduce their structures here as controlling the microstructure, porosity, phase composition evolve from selection of molecular chemistry and processing conditions such as pyrolysis temperature, gaseous environment, and humidity.[35,38–41] Such properties affect the functionalities of the PDCs as will be discussed in subsequent sections.

Silicon oxycarbide (SiOC) is a ternary Si-based ceramic system, that is composed of a mixed network of Si tetrahedrally bonded to carbon and oxygen atoms and a segregated carbon phase (free C) to form an amorphous ceramic structure. When pyrolyzed at sufficiently high temperatures, graphitic carbon and crystalline SiC also form. The presence of mixed bonds and free C in the structure prevents crystallization of the silica phase and controls oxidation resistance.[42] If additives are used, they can either enhance or hinder the conductive carbon phase formation. Thus, properties such as electrical conduction, of SiOCs, are heavily influenced by the amount, size, and distribution of the conductive phases, which are in turn determined by the precursors, additives (if there is any), and the pyrolysis conditions. Electrical conductivity will also affect SiOC's electrochemical performance as Li-ion battery anode for charge storage as well as electrocatalyst support for fast transport of charge carriers.

The silicon carbonitride (SiCN) is another ternary Si-based ceramic system, that includes Si, bonded to carbon and nitrogen atoms and a segregated carbon phase. Pyrolysis of the SiCN produce two types of carbon in the structure: non-graphitic disordered carbon and turbostratic carbon. Increasing the temperature over 1500 °C contributed to the formation of the β-SiC phase, which decreased capacity at higher temperature (>1500 °C).

One of the intriguing uses of a preceramic polymer compared to that of an organic polymer matrix composite is the conversion process of the preceramic polymer into a ceramic. During this conversion, the polymer structure rearranges, releases small molecules, and undergoes numerous reactions before the final ceramic is produced.[1,3,7,8] The initial polymer structure, the atoms, and the ratio of different atoms can have a dramatic influence on this conversion. When incorporating functionality into the final ceramic via a preceramic polymer, it is important to consider how the added material or elements will influence this evolving structure during conversion. With incorporating functionality into a ceramic via a preceramic polymer, there are numerous ways to achieve this. Often on functionality can be introduced in some of these binary and tertiary systems described above by incorporating excess carbon into the system through the selection of organic groups off the backbone and processing.[7] The focus here is on ways to incorporate functionality to these polymers, typically through the incorporation of metals. Some of the common methods to synthesis includes blending of the precursor with metal or metal oxide particles, functionalization or modification of the polymer, synthesis of metallopolymers, and chemical modification of the polymer using coordination compounds.[9,10] This perspective will not be a comprehensive review of the numerous ways to synthesize base preceramic polymers such as polysilanes, polysiloxanes, polycarbosilanes, and polysilazanes. There are numerous reviews that describe the numerous routes to produce these types of preceramic polymers.[1–3,11]

One of the simplest methods is to incorporate some sort of functional particle such as a metal or metal oxide into the preceramic polymer matrix. Depending on the type of filler, the particle can be passive to the conversion process and provides the functionality to the ceramic once it has been converted. The alternative is when the filler plays an active role in the conversion process and will react with the preceramic polymer matrix or reactive gas species during pyrolysis

to form a new phases and microstructures that can create functionality. This method has also been used to mitigate some of the shrinkage preceramic polymers undergo during conversion.[3,11] An example of this can be seen with the inclusion of particles of Ni, Fe, or Co that react with the preceramic polymer matrix to yield magnetic properties into the final ceramic. (Ni[12], Fe[13,14], Co[14]).

The other main routes involve incorporation of additional elements, typically transition metals, into the starting preceramic polymer chemistry and having those metals build up phases, nanoparticles, or domains during the conversion process. One of the common methods to do this is through the functionalization of the polymer backbone and pendant groups. This is often achieved through post-polymerized modifications in organosilicons through Si-H bond modifications, often seen in these polymers, due to the versatile and high reactivity of this bond using dehydrocoupling, halogenation, radical reactions, and hydrosilylation.[15–17] For polysiloxanes, hydrolysis and condensation of alkoxides is a common route to chemically modify a preceramic polymer. One of the advantages of this route is it is relatively straightforward to incorporate metal alkoxides such as Ti, Zr, Hf, B and Al into polymers such as polysiloxane and polysilazane.[3] With polysilazane, there is the added complexity that these alkoxides with certain polysilazanes can react with either the N-H or Si-H bonds in the polymer and produce drastically different ceramics as a result.[18]

Metallopolymers are another route to add functionality through the synthesis of preceramic polymers.[19] Metallopolymers are a viable route to form nanoparticles during conversion to add functionality and are a way to develop non-oxide ceramics. Depending on the metal incorporated into the polymer, a range of functional properties can be incorporated. This includes properties such as: semi-conductive, photo-physical, optoelectronic, and magnetic.[2] The metal is either incorporated into the backbone of the polymer or through a pendant group off the main chain

through synthesis routes such as condensation, salt metathesis, ring opening polymerization, hydrofunctionalization, and post-polymerization functionalization can form linear, dendritic, and hyperbranched structures. Each of these methods have their advantages and disadvantages. Salt metathesis for example often has high yields, are selective and rapid but often require extensive purification to remove salt waste.[20] Ferrocene-containing polysiloxanes are commonly studied due to the relatively straightforward reactions, such as ring-opening polymerization, for producing metallopolymers such as polyferrocenylsilanes. These types of systems have been very successful in producing unique magnetic properties and nanostructures.[9,19,43]

The formation of metal complexes through coordination with the preceramic polymer is a lesser utilize approach and is relatively new. One of the benefits of this approach is it can improve ceramic yield through additional cross-linking in the polymer, which often provides greater thermal stability to the polymer, along with expanding the catalog of phases and compositions that can be made with these polymers.[3] This is also particularly beneficial for non-oxide ceramic since it avoids utilizing oxides like in methods such as the use of alkoxides and sol-gel. The key with this coordination is to prevent sublimation of the metal during pyrolysis and instead have it bind to the polymer so it is retained during the conversion process. Metal coordination has been utilized in polysilazanes through the coordination of metal ions such as Fe, Co, Ni, Pt, and Cu with the numerous functional groups in polysilazane[19]. Recently the use of metal complexes has been demonstrated with polycarbosilanes through bio-inspired routes that utilized pyridyl-moieties to coordinate with Ti and Zr ions.[21]

Despite the numerous advantages of preceramic polymers, there are several additional prevalent issues with these systems that limit their use. Such issues include, challenging synthesis, molecular design, conversion efficiency, high shrinkage, limited commercial availability and high

costs. These latter two factors are partially rooted in the traditional synthesis of preceramic polymers that has often been slow, costly, and labor-intensive. Much of the research and commercialization into preceramic polymers over the last several decades have been on silicon-based ceramics such as SiOC and SiC and there is much to learn in terms of the synthesis, physics, manufacture, and polymer science with functional preceramic polymers. Even for more mature techniques such as dehydrocoupling, hydrosilyation, and condensation there are opportunities to improve the process with improvements in the yield, reduction of contamination, better catalysts or even moving away from catalysts entirely.

The need to better manufacturing of these preceramics is also necessary. Outside of numerous siloxane-based polymers, the preceramic polymer industry is quite small and the cost is quite high. Many of these processes highlight above can have dangerous reagents, require small batch sizes, are expensive and frequently contaminated with inhibitors and reaction byproducts. These synthesis methods can also slow due to the sluggish reactivity of the monomers and have poor atom economy because of the formation of large amounts of small-molecule byproducts.[3] Numerous commercial preceramic polymers contain a substantial proportion of low molecular weight oligomers that are detrimental to material processing.

While these numerous synthetic routes allow for a great deal of precision in the incorporation and design of polymer structures, the field is still greatly limited if the influence of polymer structure and composition on the transition process of the polymer into a ceramic is not well understood. Establishing this relationship would be key towards identifying and developing synthetic routes to create ceramics with specific microstructures, phases, and functionalities. This would require a great deal of effort using the numerous advanced characterization techniques discussed in Section 7 through examining the impact of the polymer on pyrolysis and transition

into a final ceramic. The synthetic techniques available allow for perturbing a polymer in numerous ways such as different types of metals, different elemental ratios, bonding, and polymer structure. Many of the described techniques above often only incorporate a single additional element or metal to the base preceramic polymers. Incorporating numerous heteroatoms could allow for additional functionalities into the ceramic and new types of structures. This would add a great deal of complexity in synthesizing and designing preceramic polymers but could add a great deal of insight in developing and designing these new systems. Several of the newer techniques such as metal coordination also allow for hyperbranched, dendritic, and even block copolymers structures into the preceramic system. These structures not only would allow for new processing opportunities but could enable further hybridization through grafting nanoparticles with these preceramic polymers to enable new phases and microstructures. The interaction between the functional nanoparticle, the grafting polymer, and the matrix is not yet well understood and there is a plethora of opportunities with the chemistry and physics that can be explored in this area. If these relationships are further understood, it would provide innumerable benefit to the control and design of future functional ceramics.

3. Electrical properties

3.1. Theoretical models and conduction mechanisms

From fundamental point of view, extensive studies have been carried out to understand the role of disordering on the localization of electronic states of amorphous materials. Amorphous materials are believed to have "tails of localized states" between the valence and conductance bands, which overlap and cause the density of states at the Fermi level to be finite.[44] Amorphous semiconductor materials can undergo electronic transport via three mechanisms: conduction in the extended states, conduction in band tails, and conduction in localized states at the Fermi levels

(E_F). At high temperatures, electronic mobility is thermally activated at the extended states (Arrhenius conduction). However, as the temperature is lowered, Arrhenius conduction is replaced by a power-law relationship between the logarithm of ohmic conductivity and temperature. Mott predicted $T^{-1/(d+1)}$ dependence of the variable range hopping mechanism (VRH), where d is hopping space dimensionality.[45,46] Movement of electrons can be modified via band tail hopping (BTH) mechanism when the electrons jump from defect level to band tail and transport back to the Fermi level.[47] When conductive additives are involved, the influence on electrical conductivity can originate from the additive-matrix interface by facilitating electron transport. When the additive content is high enough and form a percolation network, it can significantly enhance the electrical conductivity by forming conductive paths in the SiOC matrix.

3.2. DC conductivity

The DC electrical conductivity of the amorphous SiOC matrix arises due to the presence of excessive C, which forms at different temperatures. For example, during polymer-ceramic conversion, excess carbon precipitates around 400°C for $[RSiO_{1.5}]_n$ with R=C_6H_5 and around 700°C for $[RSiO_{1.5}]_n$ with R=CH_3. At higher pyrolysis temperatures (above 800°C for $[RSiO_{1.5}]_n$ with R=C_6H_5 and 1400°C for $[RSiO_{1.5}]_n$ with R=CH_3), carbon clusters grow into a percolation network.[48] This can be described according to the Motts mechanism by VRH of localized charge carriers, regular electron band conduction due to the intrinsic conductivity of turbostratic carbon (8×10^{-4} $(\Omega\cdot cm)^{-1}$) predominates.[48] In addition, polymer precursors with different side groups (Si-H, Si-CH_3, Si-CH=CH_2, and Si-C_6H_5) directly influence the C content and electrical properties of the resulting SiOC ceramics.[49] Higher C content precursors lead to higher electrical conductivity. A free C connectivity concept is proposed to understand electrical

conductivity change.[49] Overall, the electrical conductivity of SiOC is determined by the concentration of carbon clusters.

Different fillers and secondary phases can be introduced to enhance electrical conductivity.[50–54] Among these, TiC possesses an electrical conductivity of 147 $S \cdot m^{-1}$ and high thermal stability (melting point 3160°C).[55] However, in air TiC can only be used up to 400°C.[56] For $MoSi_2$, depending on the processing conditions, the electrical conductivity can be changed in opposite directions. At low temperatures a large difference in thermal expansion between the polymer and the as-added filler results in an increase of resistance from 0.05 Ω·cm to 560 Ω·cm from 20°C to 680°C. At high temperatures carburization reaction of the filler (formation of Mo_2C) on the particle surface resulted in contact formation and percolation transition, giving rise to a resistance lower than 10^{-3} Ω·cm above 1000°C.[57] The $SiC_xO_{2(1-x)}/TiO_xC_y$ ceramics reveal a maximum electrical conductivity of 10 $S \cdot cm^{-1}$. The conductivity increases with Ti doping and reaches a maximum for the composition with 30 wt% Ti precursor.[58] In Lu et al, TiO_2 nanoparticles have been introduced into the polyhydromethylsiloxane (PHMS) plus divinylbenzene (DVB) precursors.[51] SiOC–TiC_xO_y composites are made utilizing the reaction between TiO_2 nanoparticles and the free carbon in SiOC.[51] The highest electrical conductivity is 5.03 $S \cdot cm^{-1}$ at 400°C measurement temperature. However, the common problem for the polymer precursor and particle additive mixing approach is incomplete conversion of TiO_2 to TiC by forming a series of TiC_xO_y intermediates and thus electrical conductivity compromise.

To address this problem, pyrolysis of polysiloxane and titanium (IV) isopropoxide (TTIP) has been carried out at 1200°C –1400°C to form TiC, which leads to high electrical conductivity at elevated temperatures; the maximum conductivity is 1176 $S \cdot cm^{-1}$ at 950 °C, which is the first reported value of >1000 $S \cdot cm^{-1}$ conductivity for Si-O-C-Ti ceramics.[59] However, too high a

pyrolysis temperature, such as 1400°C, can potentially 'destabilize' the Si-O-C-Ti system by consuming the free carbon and result in lower conductivities. For SiTiOC derived from pure polysiloxane and titanium isopropoxide (TTIP) modified polysiloxane using flash pyrolysis,[60] The electrical transport follows an amorphous semiconductor mechanism. Flash pyrolyzed nanocomposite with a Ti:Si molar ratio of 0.20 exhibits the highest electrical conductivity of 0.696 $S \cdot cm^{-1}$.[60] Another successful example of co-pyrolyzing polymer precursors for conductive SiOCs is polysiloxane with the addition of nickel 2,4-pentanedionate to make Ni-containing silicon oxycarbide (SiOC–Ni). The key aspect is to use water vapor during the pyrolysis in order to suppress the formation of NiO and thus obtain well dispersed Ni species in the SiOC matrix. The composites exhibit desirable electrical conductivity up to ~900°C with the highest electrical conductivity at ~247 $S \cdot cm^{-1}$.[61]

Ti_3C_2 perfectly showcases a layered structure, outstanding electrical conductivity (as high as 6500 $S \cdot cm^{-1}$-8000 $S \cdot cm^{-1}$),[62–64] tunable active surface, and excellent mechanical strength. The multilayered structure of Ti_3C_2 can be retained up to 900°C in an inert gas.[65] When Ti_3C_2 and polysiloxane are integrated into one system at the liquid precursor stage, the polysiloxane precursor can potentially infiltrate in-between the Ti_3C_2 layers and achieve nanoscale homogeneity. At <1000°C pyrolysis, Ti_3C_2 should be retained. At >1000°C pyrolysis, Ti_3C_2 should consume the excessive C in the SiOC system and form TiC-SiC interlocking structures. polysiloxane and Ti_3C_2 derived SiOC-TiC composites should drastically increase the electrical conductivity since TiC is highly conductive.

Fig. 2a shows the DC conductivity (σ) of a 0.05 wt% Ti_3C_2-SiOC sample from room temperature to 1000°C in Ar. It should be noted that the Ti_3C_2 content is extremely low in this work. The conductivity increases exponentially with temperature. At lower temperatures (up to

400°C), the electrical conductivity increases with the Ti_3C_2 content increase, at 16.7%. At high temperatures (from 400°C to 1000°C), the electrical conductivity continues to increase, reaching the highest value of ~17.93 x 10^{-2} S×cm^{-1} at 1000°C.

The conductivity result, *log (σ(T))* as a function of $T^{-0.25}$ (Fig. 2b), shows good linear fit for the Ti_3C_2-SiOC sample between room temperature and 400°C. This means that below 400°C, phonon assisted tunneling or hopping takes place in the Ti_3C_2-SiOC samples. However, as the temperature increases to >400°C, the DC electrical conductivity shows an Arrhenius-like behavior; the charge carriers overcome the potential barrier by thermal activation; and high mobility carriers (electrons) are activated to the extended states.[47] The activation energy (E_a) calculated using the Arrhenius equation is 0.26 eV.

Similar to Ti_3C_2, graphene nanoplatelets have been incorporated into SiOC pyrolyzed at 1000°C. The electrical conductivity increases by four orders of magnitude (from 9.89 x10^{-5} S·cm^{-1} to 1.2 x 10^{-1} S·cm^{-1}) by addition of 6 wt% graphene.[65] Similar effects from graphite, carbon black, lamp black, active carbon, and graphene on SiOC electrical conductivity have also been reported with spark plasma sintering, with the additive measure to enhance the density of the samples.[10,66,67]

3.3. AC conductivity

The electrical conductivity of the SiOC-based systems can also be evaluated using AC conductivity measurements. It can provide understanding to the behaviors of different phases and interfaces and elucidate the conductivity mechanisms in the system. During the AC conductivity measurement, a current is applied and the impedance has real and imaginary parts. The high frequency or low *Z*' semi-circle represents the ohmic resistance (R_W) while the low frequency range or high *Z*' semi-circle represents the resistance due to both the R_W and polarization resistance (R_p).

Previous studies carried out on pure SiOC show two semi-circles due to the charge transport of the matrix and free carbon clusters.[60] Fig. 3 shows the real and imaginary impedances as a function of frequency for the flash pyrolyzed SiC-TiC nanocomposites (with the additive of TTIP) at room temperature. The real part (*Z'*) of all these samples shows frequency dependent throughout the frequency measurement range, indicative of a capacitive behavior. The *Z'* value approaching the lowest testing frequency can be deemed as the DC resistance. With the increase of the TTIP content, the flat-to-dispersive transition in *Z'* moves to a higher frequency with a wider plateau region. This reflects a weakened capacitive characteristic and a more conductive nature of the material. In addition, the imaginary part (*-Z''*) exhibits a sharp peak at the frequency where the sudden decrease of Z' occurs (typically called characteristic frequency f_C), featuring a dielectric relaxation process.

For the Ti_3C_2-SiOC system under an AC electric field, the electron transport takes place via an inductor-resistor-capacitor mode in series. Even at only 0.05 wt% Ti_3C_2 content, the Ti_3C_2-SiOC samples show one semi-circle (Fig. 4a). The major charge transport in Ti_3C_2-SiOC takes place via Ti_3C_2 or Ti_3C_2-SiOC-C interface while the contribution of the SiOC matrix is minimal. The inductor impedance (Ti_3C_2) increases with the frequency and Ti_3C_2 acts as a short circuit at low frequencies. The Ti_3C_2-SiOC-C interface comprises a capacitor and a resistor in parallel, which are in turn in series with Ti_3C_2. The capacitor (interface) impedance decreases with frequency increase while the resistor (ohmic resistance) is independent of the frequency. The high temperature electrical conductivity from 600°C to 1000°C is due to thermally activated jumping of electrons to the conduction energy band (ohmic resistance).

Fig. 4b shows both the measured and the curve fitted (using the equivalent circuit shown in the insert) impedances of the 0.05 wt% Ti_3C_2-SiOC ceramics. The equivalent circuit comprises an inductor and an ohmic resistor (R_W) due to the presence of exfoliated layers of Ti_3C_2 in the SiOC matrix. The capacitor and polarization resistor arise due to the Ti_3C_2-SiOC (R_p) interface. The Ti_3C_2-SiOC-C interface comprises a capacitor and a resistor in parallel, which are in turn in series with Ti_3C_2. The capacitor (interface) impedance decreases with frequency increase while the resistor (ohmic resistance) is independent of the frequency. However, the capacitor impedance (Ti_3C_2-SiOC-C interface) diminishes above a certain frequency and is smaller than that of the resistor impedance (Ti_3C_2-SiOC-C interface), wherein the resistor impedance acts as a short circuit and removes the resistor component from the circuit. Therefore, the contribution of the capacitor to the electrical impedance is negligible. In all cases, the contribution of carbon conduction is minimal or negligible compared to that of the Ti_3C_2-SiOC-C interface or Ti_3C_2.

Fig. 5a shows the real impedance change with frequency for the Ti_3C_2-SiOC system. As expected, from room temperature to 600°C, the low frequency range exhibits only the DC resistance. However, at high frequencies there is an inflection point, indicating the flat-to-dispersive transition in Z'. At temperatures higher than 600°C, the system exhibits a capacitance behavior, likely due to the contribution of the Ti_3C_2-SiOC-C interface. The temperature increase from 600 to 1000°C does not cause any appreciable change in real impedance, which is indicative of DC resistance. This means that high temperature decreases the activation energy for the charge carrier jumping to the conduction band for the 0.05 wt% Ti_3C_2-SiOC material.

Fig. 5b shows the changes of the imaginary impedance (Z'') with frequency for the 0.05 wt% Ti_3C_2-SiOC from room temperature to 1000°C. It exhibits an increasing trend, a peak, and

then a sudden drop with frequency. The frequency at which the slope changes is termed as characteristics frequency (f_c), which indicates the dielectric relaxation process.

For the Ti_3C_2-SiOC system, the imaginary component of the impedance as a function of frequency shows only one peak irrespective of the Ti_3C_2 content (Fig. 5b). The characteristic peak shifts to higher frequency with temperature, which suggests that more than one relaxation phenomenon is present. The 0.05 wt% Ti_3C_2-SiOC has peaks at 26 $x10^3$ (room temperature), 35 $x10^3$ (200˚C), 56 $x10^3$ (400˚C), and 489 $x10^3$ Hz (600˚C). At high temperatures, the contribution is affected due to significant ohmic resistance of the SiOC matrix and the Ti_3C_2-SiOC-C interfacial resistance.

For pure SiOC and SiOC ceramics with graphene oxide (GO) and multiwalled carbon nanotubes (MWCNT), the Nyquist plots from room temperature to 250°C in the frequency range of 1 mHz – 1 MHz show similar trends.[68] All the systems are composed of one semicircle, which is indicative of the presence of bulk resistance and capacitance. The pure SiOC also exhibits a single semi-circle, unlike the PSO-derived SiOC observed in our work, as shown in Fig. 4. This could be due to the presence of a negligible amount of carbon clusters. Addition of GO and MWCNT fillers enhance the percolation pathways for conduction. With increase in temperature, the semi-circle shifts towards the origin, indicative of a decrease in bulk resistance, i.e., at room temperature it is 50 MΩ, 80 kΩ, and 7 kΩ for SiOC, 5 wt% GO-SiOC, and MWCNT-SiOC respectively.

3.4. Outlook

As discussed, the electrical conductivity of polymer-derived ceramics, e.g., SiOC, depends to a large extent on the types of electronic carriers as well as the amounts and distributions of such carriers. Since most of the polymer-derived ceramic systems are carbon-excessive, the electrical

conductivity often is determined by the free carbon amount. The pyrolysis temperature has a significant effect in this regard since it directly determines the carbon phase type and amount. A higher amount of carbon leads to higher electrical conductivity. A higher content of graphitic carbon (vs. amorphous carbon) also has the same effect. However, a high carbon content can lead to high temperature material instability. When conductive additives are introduced, the contribution to the overall electrical conductivity depends on the conductivity of the additive species vs. that of carbon. If the former is more conductive, then the electrical conductivity behaviors will be determined by the additives. In general, polymer-derived ceramics have lower electrical conductivity than metals. This is especially the case when the conducting species do not form a percolative network. The main advantage of such systems is their high temperature stability, low thermal expansion, and corrosion resistance when moderate electrical performance is desired.

4. Magnetic properties

4.1. Magnetism in SiOC

Literature reports on magnetic properties of SiOC ceramics are scant. Intrinsically, SiOC species do not have magnetism. Magnetic additives need to be introduced into the SiOC matrix, such as Fe_3O_4, γ-Fe_2O_3, $MnFe_2O_4$, $CoFe_2O_4$, FePt, CoPt, NiPt, Co, and Fe, to induce magnetism.[69] However, additives should not react with SiOC or convert into undesired compounds during pyrolysis. Under such constraints, viable species are scant and limited to Ni and iron silicides thus far.[70]

Various compositions of Ni-containing SiOCs have been prepared, for which Ni (II) 2,4-pentanedionate was used as the Ni source. The volume ratio of Ni relative to cross-linked polysiloxane is 1, 2, 3, and 4 (Fig. 6).[61] The magnetic hysteresis of Ni-SiOC prepared at 800^0C,

900^0C and 1100^0C are shown in Fig. 6. This study reveals that saturation magnetization (M_s) increases with pyrolysis temperature while squareness ratio (M_r/M_s) increases with Ni concentration at lower pyrolysis temperatures. The hysteresis loop is sharp and narrow, indicating soft ferromagnetic behavior. Magnetization (M_s) is purely due to Ni particles; at 900^0C pyrolysis temperature, M_s = 7.14 emu·g^{-1}. Further increase in pyrolysis temperature results in enhanced NiO formation and decrease in magnetization. Ni-modified SiOC ceramics pyrolyzed at 900°C exhibit enhanced magnetic properties compared to that pyrolyzed at 1100^0C.

The squareness ratio is defined as the ratio of the magnetic field at 90% of the remanent magnetization to coercivity (H_c). The squareness value in the Ni-SiOC ceramics ranges from M_r/M_s = 0.07 to 0.35 for the 800^0C pyrolyzed samples, while for the 900^0C and 1100^0C pyrolyzed samples M_r/M_s decreases with the Ni concentration (M_r/M_s = 0.28 to 0.10). It is well known that for randomly oriented, identical particles, the ideal Stoner-Wohlfarth value is 0.5.[71] In Ni-SiOC ceramics, it is below 0.5 irrespective of the Ni concentration and pyrolysis temperature. In general, Ni crystallite size and its distribution and concentration in SiOC ceramics play a vital role in the magnetic behavior. Therefore, Ni crystallite size should be controlled and the NiO formation in SiOC ceramics should be minimized.

The magnetic behaviors of Fe-SiOC ceramics are studied from hydroxy- and ethoxy-substituted polymethylsilsesquioxane precursor wherein 50 wt% $Fe(acac)_3$ has been used as the Fe source.[72] Ferromagnetic behavior of SiFeOC ceramics exhibits a narrow hysteresis loop with smaller coercivity and remanence. The magnetization is dependent on the pyrolysis temperature (Fig. 7). SiFeOC ceramics prepared at 1500^0C exhibit the largest magnetization value of 26.0 emu·g^{-1} while the samples pyrolyzed at 1000^0C and 1400^0C result in magnetization values ranging between 1.63 to 2.87 emu·g^{-1}. However, the intrinsic mechanism leading to enhanced

magnetization for the samples prepared at 1500^0C samples is not understood. The most probably reason could be due to the stabilization of Fe_5Si_3 at high temperatures. In general, the magnetization process is controlled by movement of domain walls or domain nucleation, any hinderances (localized stress or non-magnetic phases) could result in lower magnetization. In SiFeOC ceramics, the magnetic phases, Fe_3Si and Fe_5Si_3, are embedded in the SiOC matrix. Therefore, the resistance in domain walls motion/rotation is hindered by the Fe_5Si_3-SiOC and Fe_3Si-SiOC interfaces. As expected, lowering the concentration of Fe_5Si_3 (3.64 emu·g^{-1}) and Fe_3Si (0.74 emu·g^{-1}) do not improve the magnetization values due to multi-grain domain structure. Methods need to be developed to address domain wall rotation in the SiOC matrix.

Methods are also developed to mix iron silicate particles of 9 μm size directly in polymer precursor (PSO) along with sacrificial poly-methyl-methacrylate of 25 μm size to form SiOC foams with magnetic functionality.[73] The iron silicate particles undergo phase transformation and melting and result in fine cubic Fe_3Si particles embedded in the SiOC ceramic matrix. The hysteresis loop is narrow for all composition and shape of the loop does not change appreciably with pyrolysis temperature. With the iron silicate content increase, the magnetic response increases. Further, the squareness value was less than 0.01 and temperature does not have any effect. The magnetic coercivity value ranges between 4.0 to 16.2 Oe, which is small and dependent on the concentration of iron silicate. The saturation magnetization is in the range of 9.5–17 emu·g^{-1}. Again, the iron silicate filler-SiOC exhibits the presence of multidomain grain structures. One interesting observation is that iron silicate does not react with the polymer precursor. This is important because the magnetic properties can be enhanced by using grains with unique outer planes and aspect ratios.

4.2. Outlook

Overall, research on magnetic SiOC systems is rather limited. Magnetism relies on the externally added or *in-situ* precipitated magnetic species. The corresponding size and distribution along with the intrinsic magnetism determines the resulting properties of the composites. In general, filler-induced SiOC magnetic materials are weak soft magnets, mainly because the additives are embedded in the SiOC matrix, often with low amounts. Viable magnetic species are also limited due to the reaction potential with the SiOC matrix during high temperature pyrolysis.

5. Energy conversion and heterogeneous catalysis

The tunability of PDCs from an array of polymeric precursors provide for a flexible chemical approach to materials design for heterogenous catalysis and energy conversion applications. The need for enhanced selectivity is a key driver for utilizing materials with precise chemical tuning to develop catalysts and catalyst supports. Heterogeneous catalysis involved in conversion of greenhouse gases typically require active site-specific chemistry that enables the control of parameters such as *d*-band center alignment and catalyst support porosity. Electrocatalysis, similarly, relies on specific control of active sites (i.e. via adatoms,[74,75] exposure of specific nanostructured facets,[76–80] and nanostructure morphologies[81]) to increase faradaic efficiency and selectivity of products. This portion of the perspective will focus on the role of processing and chemical design in producing targeted polymer-derived ceramics microstructures and nanocomposites for energy conversion. We will also discuss the potential synergy of incorporating additional filler precursors into preceramic polymer matrices for providing both active site centers and governing intricate microstructures with graded porosity[82–85] or gyroidal[86] pathways for controlling gas adsorption.

5.1. Controlling Porosity

Porosity (i.e. pore size, surface area, pore structure, permeability, and mechanical stability) in PDCs have typically been controlled via processing conditions (i.e. gas environment, precursor chemistry). There is a wide range of applications beyond ceramic supports for catalysis such as water pollution mitigation[87] and biomorphic melanin[88]. For catalytic materials support, permeability of gases is key for facilitating efficient flow of reactants and effluent. Control of porosity and pore sizes (i.e. micropores, pore diameter < 2 nm; mesopores, pore diameter 2 nm < pore diameter < 50 nm) in polymer derived ceramics offers the same catalytic support with enhanced gas permeability and conversion kinetics. Porosity tunability is achieved through altered processing conditions and has been heavily investigated in the 1990s and early 2000s as the microstructure has direct impact on the material's mechanical properties.[6,84,89,90] Design of processing conditions to target ordered[91] or hierarchical porosity in PDCs enables fast kinetics of gas adsorption while maintaining high mechanical strength as observed in biomorphic cellular designs.[92] The high purity of precursors, reduced processing temperatures as compared with powder technologies, and combination of organic and inorganic precursors[93] results in a large array of porous structures that can be achieved. For example, pyrolysis of preceramic polymer and block copolymer blend processed by freeze casting resulted in hierarchical porosity with bimodal pore size distribution in the range of 10 nm – 100 nm and 10 μm – 100 μm.[85] Reduction of pore size to micropores to increase connectivity of the ceramic can potentially be achieved by adjusting relative organic polymer block size.[94,95] Sourcing plant-based biowaste materials such as rice rusk,[96] is another route for sustainably processing preceramic polymers. Hierarchically porous SiOC was produced using rice rusk as the porogen. Similarly, kraft pulp paper and allylhydridopolycarbosilane produced tunable open porosity between 15% and 93%.[97]

Accessing gyroidal, porous microstructure for heterogeneous catalytic applications is another avenue for controlling gas flow in support materials. SiON monoliths with gyroidal mesoporous microstructure ($Ia\bar{3}d$) and pore sizes of ≈9.4 nm have been produced from pyrolysis of polysilazane blends (poly(methyl-vinyl-silazane)) with self-assembled poly(isoprene)-b-polystyrene-b-poly(N,N-dimethylamino ethyl methacrylate (PI-PS-PDMAEMA)).[86] The symmetric cubic gyroid structure enables isotropic volume contraction during pyrolysis and prevents microporosity formation. These monolithic mesoporous ceramics offer additional suitable porous microstructures for using catalyst support to control gas flow kinetics. Furthermore, processing with organic block copolymer templates have value-added prevention of structural collapse by enabling release of gaseous by-products during pyrolysis.

For coatings and applications in which form factor is a key component, planar porous ceramic supports are configurations that offer high biaxial flexural strength in addition to controlled porosity. PDCs also offer increased flexibility, which is an additional advantage for resistance to atomic oxygen attack and erosion of materials in lower Earth orbit.[98] Konegger and co-workers have demonstrated microporous polysilazane-derived ceramic supports with pore sizes of ≈1 μm[99] with planar geometry[100] with high temperature thermal stability in oxidizing and reducing atmospheres. Such cycling of oxidizing and reducing environments is typical in heterogeneous for catalyst preparation and subsequent reaction. A bilayer combination of ordered mesoporous or macroporous structure on one side with gradient porosity towards the second surface for directional control of gas flow.

For homogeneous liquid reactions, liquid-liquid interfacial wettability along with hydrophobicity or hydrophilicity can be controlled with the release of organic groups in the preceramic polymers during pyrolysis. Cellular PDC foams can be produced polysiloxanes and

polysilsesquioxanes.[101] During pyrolysis of polymethylsiloxanes and polymethylphenylsiloxanes by Cerny et al,[102] water contact angle wad adjusted by controlling cleavage of side chains. Since Si-methyl bond energy is higher than that of Si-phenyl bond by 103 kJ/mol, the phenyl groups were cleaved at lower temperatures during pyrolysis. This resulted in control in the concentration of organic functional groups during pyrolysis between T = 773 K and T = 1123 K. Coatings with gradient surface concentration can also be tuned with a temperature gradient across the sample to tune wettability as a function of film depth.

Hierarchically porous PDC materials with metal embedded catalysts offer advantages for controlling reaction activity and selectivity, which is particularly useful for conversion of gas reactants as well as producing dense fuels such as hydrogen. Hierarchically porous SiCN with Pd catalysts oxidized methane at higher conversion rates at > 400℃ relative to unporous SiCN.[103] Conversion rates for CO_2 methanation for Ni particles in microporous and microporous SiOC monoliths produced from 3-aminopropyltriethoxysilane precursors.[104] Such conversion rate enhancement, relative to metal nanoparticle impregnation method, was attributed to formation of micropores and advantageously resulted in higher surface area (400 m^2/g) and enhanced mass transport. Selectivity towards methane was a result of smaller Ni particles, which were also well-dispersed due to the type of Ni precursor (nitrate relative to higher chelating ligands such as acetylacetonate). Hydrocarbon oxidation from Cu-containing SiCN PDCs can selectively convert cycloalkanes to ketones.[105] Similar to Ni embedded SiOC,[104] the *in-situ* incorporation of Cu is key for metal particle size control, which directly impacts activity and selectivity. Expanding the targeted set of reactions beyond selective oxidation and methanation, the Fischer-Tropsch synthesis, $(2n+1)H_2 + nCO \rightarrow C_nH_{(2n+2)} + nH_2O$, is an important process for producing high value hydrocarbon liquid fuels, particularly for $n > 1$. Lower olefins, liquid fuels, waxes, and oxygenates

are targeted materials for the rubber, transportation, lubrication, and cleaning industries.[106] Ni, Fe, and Co have been high activity catalysts due to their relatively lower cost than Ru. Embedding Fischer-Tropsch catalysts such as the aforementioned *3d* transition metals into ceramic matrix support such as SiOC and SiCN consists of additional advantage that the support may promote catalytic activity, as demonstrated by Fe-based catalysts and a library of supports (i.e. carbon-based,[106] metal organic frameworks,[107,108] silica,[109] and alumina[110]).

While conventional metal organic frameworks may offer higher gravimetric metrics for hydrogen storage,[111] economies of scale benefit ammonia manufacturing,[112] which is an advantage for using polymer-derived ceramics. The water-gas shift reaction ($CO + H_2O \leftrightarrow CO_2 + H_2$) is one method for hydrogen production towards ammonia synthesis and can be used to aid with increasing fuel cell efficiency by increasing hydrogen production and decreasing CO production. Industrial scale catalysts typically consist of *3d* transition metal oxides combined with structural promoters and dispersant support materials, which may also be Groups 2, 12, 13-based oxides.[113] PDCs offer advantages of single-source preceramic polymer synthesis routes for controlling size of embedded catalyst particles along with hydrogen storage capabilities.

For electrocatalysis, the high porosity and doping can enhance mass transfer and charge transfer while providing increased active sites. Such strategies have been demonstrated to be effective for increasing electroreduction of oxygen (ORR) with activated N-doped porous carbon spheres.[114] Nanocomposites of graphene oxide (rGO) and boron-modified polyvinylsilazane based ceramic increased transport of charge carriers and decreased onset potential of -340 mV vs. reversible hydrogen electrode (RHE) for hydrogen evolution reaction (HER).[115] PDCs can be high-performing electrocatalyst nanocomposite supports (i.e. with rGO) due to the ability for controlling O, N, and B content. These dopants have the demonstrated potential to increase electrical

conductivity in the support and promote catalysis while maintaining chemical stability in highly corrosive media.

5.2. Outlook

PDCs with metal centers embedded from single source precursors[23,88] and processing methods can enable both chemical and microstructure tuning simultaneously. Incorporation of transition metals and metal oxides have been investigated for functionalizing PDCs with properties such as magnetism (Ni,[61] Fe,[116,117] Co[117]). These *3d* transition metals are also particularly attractive as they can modulate the *d*-band center for enhancing catalytic activity (i.e. CO oxidation) and reduce use of precious metals such as Pt and Pd, typically used in such reactions.[76,118] The incorporation of metal salt precursors with preceramic polymers throughout crosslinking and pyrolysis can lead to advantageous enhanced catalytic activity due to hydrophobicity of catalyst surface as compared to conventional impregnation of catalyst on ceramic support methods.[104] Thus, we need to build upon the library of existing methods for incorporating transition metals into ceramic matrix[117,119–126] for enhanced, selective catalytic conversion of fuels. Even inclusion of nanoparticles into preceramic polymer matrix have demonstrated to enhance catalytic activity in the hydrolysis of sodium borohydride in high pH conditions. The roles of metal salt selection, sacrificial organic block copolymer templates, gas environment, and additives such as water need to be investigated systematically to establish strategies for producing targeted catalyst morphologies embedded in ceramic matrix with controlled hierarchical and/or graded porosities (Fig. 8, significantly adapted from Choudhary and co-workers[92]).

6. Energy storage

Electrochemical energy storage systems (EESS) are critical for sustainable alternative energy sources. In the last few decades, many scientific research studies have focused on developing high capacity, rechargeable devices with long life cycles. The challenge for researchers has been to develop small, light-weight systems that have high energy and power densities during their long cycling time to accommodate real-life applications. In this regard, PDCs have emerged as the electrode materials of choice for secondary batteries to replace traditional graphite-based electrodes.

The electrochemical properties of ceramics derived from a molecular precursor were first introduced by Dahn et al. in the 1990s.[127,128] For the following two decades, researchers have diligently studied PDCs' ability to reversibly intercalate metal-ions. The mixed bond structure in the final amorphous ceramic and the conducting carbon phase, especially in silicon-based PDCs, control the electrochemical properties of PDCs in reversible storge systems.[129,130] PDC performance as electrodes in electrochemical energy storage devices has also been investigated systematically using various fabrication techniques. In addition to conventional bulk powder-based film, thinner films fabricated by depositing preceramic polymer onto a current collector, followed by pyrolysis, have shown promise to achieve high storage capacity of PDC electrodes.[131] The used of additive manufacturing technology to fabricate complex and lightweight PDC electrodes has also been reported,[132] and electrospinning technique has been utilized to fabricate flexible, wearable, cloth-like PDC electrodes to achieve outstanding electrochemical performance.[133] All these techniques enable the hierarchical porosity and intrinsic conductivity in the PDCs, which can successfully buffer volume changes of the electrode during charge/discharge

cycles. The following sections describe the electrochemical performances of various PDCs synthesized using different techniques in metal-ion batteries.

6.1. PDCs in electrochemical energy storage systems

The application of PDCs as active electrode materials in EESSs such as lithium-ion batteries (LIBs) and sodium-ion batteries (SIBs) is detailed in the following subsections. The discussion focused on how performance parameters and other essential criteria: structure of molecular precursors, pyrolysis temperature, and pyrolysis environment play important roles in the electrochemical performance of the PDC electrodes. Primarily, PDCs are used as negative electrode materials (anodes) in the EESS, which will be our main focus in this section.

6.1.1. PDCs in Li-ion batteries

LIBs extensively utilize Si-based nanostructures due to their favorable properties towards lithium storage, (e.g., high theoretical capacity of 4200 mAh g^{-1}, which is almost ten-fold higher than traditional graphite electrodes)[134,135] and because Si has low charge/discharge potential (~0.5 V vs. Li/Li^+).[136] However, the formation of Li-Si alloy is less reversible in room temperature, and Li insertion into Si results in 400% volume expansion of the Si lattice,[137,138] which contributes to electrode pulverization, reduced electrical contact, and severe capacity fading. One of the ways to overcome this problem is to utilize Si-based PDCs instead of Si in its bulk form. Current state-of-the-art applications of Si-based PDCs can store lithium reversibly in the potential range of 0-3 V and provide a specific capacity of 900 mAh g^{-1} with a high coulombic efficiency of 99%. In addition, the porous microstructure of PDCs provides high surface area, and structural stability during lithiation and delithiation. Among several alternatives, silicon oxycarbide, derived from polysiloxanes, and silicon carbonitride, derived from polysilazane, are the most promising PDCs as electrode materials. The most common synthetic process of SiOC and SiCN, and their charge-

storage mechanism is shown in Fig. 9a - Fig. 9b. Maximum capacity is achieved in the amorphous ceramic phase as shown in Fig. 9c, where the SiO_2 and SiC mixed bonds co-exist with the free C domains.

6.1.2. Li-ion storage in SiOC

Maximum capacity is achieved in the amorphous ceramic phase as shown in Fig. 9c, where the SiO_2 and SiC mixed bonds co-exist with the free C domains. Since Wilson et al. reported bulk SiOC as potential anode material in LIBs in 1994,[127] continuous efforts have been made to apply SiOC anodes for Li-ion storage. Wilson et al. showed that amorphous SiOC derived from two different polysiloxanes achieved a specific capacity near 600 mAh g^{-1} when the majority of capacity were below 1.0 V vs Li/Li^+. In 1997, Xing et al. studied over 60 siloxane polymers to derive various compositions of SiOC samples at a temperature of 1000°C.[128] They showed that the presence of carbon in amorphous SiOC is necessary to provide a path for Li ions and electrons and to reversibly react with lithium. Xue et al. showed that irreversible capacity, associated with the first-cycle charge/discharge of a SiOC electrode in LIBs, increased with the increase of silicon and oxygen contents.[139]

Dibandjo et al. studied the lithium insertion/extraction properties of dense and porous SiOC ceramics.[140] Porous SiOC was achieved by etching dense SiOC using a 20 vol% hydrofluoric acid (HF) solution. The initial cycles were run at a current density of 18 mA g^{-1}, and then the current density was increased to 36 mA g^{-1}. Although both dense and porous SiOC provided > 600 mAh g^{-1} as first cycle capacities, the porous sample showed a stable electrochemical response up to 30 cycles while the dense sample capacity dropped to zero after 10 cycles. Kaspar et al. studied the influence of pyrolysis temperature ranging from 900°C to 2000°C.[141,142] Results showed that increasing temperatures caused the free C phase to organize toward ordered configurations, and

amorphous SiOC resulted in SiC crystals. In addition, decomposition of the SiOC network at increased temperature decreased the stability of the free C phase. As a result, the reversible capacity dropped from 660 mAh g^{-1} at 900 °C to 80 mAh g^{-1} at 2000 °C.

Ahn et al. utilized the coulometric titration technique to study hysteresis in SiOC ceramics.[143] They measured the polarization potential of hysteresis to be 250-500 mV, which occurred at the anode-electrolyte interface and was proportional to the cycling rate. Coating the active SiOC with a few layers of alumina shifted the hysteresis curve by ~50 mV, indicating that hysteresis was due to the kinetics and thermodynamic limitations of Li^+ ions diffusion in the SiOC system. Kaspar et al. showed that the presence of carbon influences electrical conductivity and thus capacity of the SiOC electrode in LIBs.[144] Materials with carbon content < 20 wt.% showed electrical conductivity of 3×10^{-8} S m^{-1}, and their initial capacity faded rapidly with cycling. However, materials with higher C contents had up to 2.2 S m^{-1} electrical conductivity and demonstrated stable specific capacity of 500 mAh g^{-1} after 60 cycles.

Sun et al. incorporated the first-principles theoretical approach to study lithium storage in SiOC.[145] They suggested a two-step process: Li ions are first absorbed in the nanovoids, and then they get absorbed in SiOC tetrahedral units, free C phase, and defects. Charge transfer occurred in the defects and edge of five or seven carbon rings, whereas in the SiOC system charge transfer occurred primarily around the oxygen and carbon atoms.

6.1.3. Li-ion storage in SiCN

Similar to SiOC, the high capacity of the SiCN is achieved towards the center of the amorphous ceramic phase as shown in Fig. 9d. Liebau-Kunzmann et al. were among the first to suggest the use of SiCN as potential anode for LIBs.[146] They synthesized lithium-containing SiCN

via lithiation of polysilazane. Li bonded to C and N in the SiCN system were found after pyrolysis at 1100 °C. Their results affirmed the potential use of a SiCN anode in LIBs.

Su et al. investigated the electrochemical properties of SiCN in LIBs, where SiCN were obtained at various pyrolysis temperature.[147] Results showed that amorphous SiCN obtained at 1000-1300 °C had a free C phase and showed a high first cycle capacity of 608 mAh g^{-1} - 754 mAh g^{-1}. However, the SiCN derived at 600-800 °C contained organic groups, and the SiCN derived at 1400-1500 °C contained SiC crystallites, which exhibited much lower specific capacities than the amorphous SiCN. Graczyk-Zajac et al. studied the performance of SiCN in LIBs derived from polysilazane at five temperatures: 1100°C, 1300°C, 1500°C, 1700°C, and 2000°C.[148] The authors showed that carbon-rich SiCN prepared at 1300°C exhibited excellent stability during cycling and provided ~300 mAh g^{-1} after 60 cycles. The samples synthesized at 1100°C and 1500°C both showed ~100 mAh g^{-1}, whereas 1700°C and 2000°C samples reached <100 mAh g^{-1} and ~200 mAh g^{-1}, respectively after 60 galvanostatic cycles.

Liu et al. studied the variation of pyrolysis environment using Ar and H_2 environments.[149] The H_2 atmosphere demonstrated higher carbon content and reversible capacity. DVB was used with polysilazane as an additional carbon source, the carbon content increased from 9.9 wt.% to 49.3 wt.%, resulting in increased specific capacity from 136 mAh g^{-1} to 574 mAh g^{-1} for SiCN as an anode in LIBs.

Feng et al. investigated five different polymer precursors to synthesize SiCN with various carbon contents.[150] They also studied the carbon contribution in SiCN materials during lithiation/delithiation and the reason for capacity fading. Results showed that the di-n-octyldichlorosilane synthesized poly-silyl-carbodiimide sample provided the highest carbon content, with the highest reversible capacity of 826.7 mAh g^{-1} after 100 cycles with > 97%

coulombic efficiency. The outstanding electrochemical performance of this SiCN anode was due to the formation of a stable solid electrolyte interface (SEI) layer on the anode surface, which prevented electrode cracking during lithiation/delithiation. Increased carbon content also resulted in high electrical conductivity and electrochemically reactive sites.

6.1.4. Li-ion storage in PDC/nanomaterial composites

PDC-based anodes such as SiOC and SiCN pose several drawbacks when used on their own as powder-based, thin film, amorphous, or crystalline electrodes in LIBs. High first-cycle loss, voltage hysteresis, and capacity decay are the primary disadvantages of using bare PDC materials as electrodes. Therefore, researchers have introduced nanomaterials, especially graphene or carbon nanotubes (CNTs), into PDCs to synthesize nanomaterial-based composite electrode materials. These PDC-nanomaterials composites offer reduced ionic diffusion length, high electronic mobility, and high aspect ratio.[151] For example, Konno et al. synthesized a SiOC/exfoliated graphite composite and studied the electrochemical performance in LIBs.[152] As an anode, this composite material delivered a reversible capacity of 625 mAh g^{-1} with a first cycle loss of 30%. The composite samples were pyrolyzed at 1000°C - 1300°C and all the samples showed stable performance at a high current density of 100 mA g^{-1}. Wu et al. embedded SiOC nanolayers directly into graphite to synthesize a SiOC/graphite composite electrode.[153] The graphite acted as a support to enhance the structural stability and electrical conductivity of the composite and decreased the diffusion path for lithium. The composite anode showed almost 100% capacity retention even after cycling at 5000 mA g^{-1}, while the electrode showed a diffusion coefficient of ~2 × 10^{-10} cm^2 s^{-1} and delivered a reversible capacity of 500 mAh g^{-1} over 1000 cycles at a current density of 2000 mA g^{-1}.

Feng et al. introduced CNTs into SiCN by pyrolyzing polysilylethylenediamine with multi-walled CNTs at 1000°C.[154] The as-synthesized SiCN/CNT composite, which was used as anode material in LIBs, delivered a high discharge capacity of 1176.6 mAh g^{-1} at a current density of 0.2 mA cm^{-2}. The 3D network of CNTs provided an enhanced electrical conductivity and a stable structure to the composite electrode. The electrochemical performance of the SiCN/CNT composite was much higher than the capacity of pure SiCN, CNTs, and commercial graphite electrodes.

David et al. coated an aluminum-modified polysilazane on the surface of CNTs to synthesize a Si(Al)CN/CNTs composite electrode material.[155] The as-prepared composite electrode showed high rate capability and cycling stability as LIB anode, due to the enhanced electrical conductivity (by 7 times compared to SiCN), when SiCN interfaced with aluminum and CNTs. The Si(Al)CN/CNT electrode exhibited stable specific capacity of 577 mAh g^{-1} at a current density of 100 mAh g^{-1} and 400 mAh g^{-1} at an extreme current density of 10,000 mA g^{-1}.

Huang et al. integrated MnO nanoparticles into a SiOC matrix to investigate the electrochemical performance of SiOC/MnO electrodes.[156] MnO has high theoretical capacity (755 mAh g^{-1}), low volage hysteresis (<0.8 V), and low plateau voltage (1.032 V) in LIBs. Introducing MnO into the SiOC ceramic resulted in stable performance with high capacity. The SiOC/MnO composite anode in LIBs delivered a high reversible capacity of 770 mAh g^{-1} at a current density of 100 mA g^{-1} after 200 cycles. In another study, Idrees et al. introduced nitrogen sulfur dual-doped graphene sheets (NSGs) into the Si(B)CN.[157] NSGs were introduced into pyrolyzed Si(B)CN using the ball milling technique. When tested as an anode in LIBs, the as-prepared Si(B)CN/NSG composite exhibited a high specific capacity of 785 mAh g^{-1} after 800 cycles at a current density

of 450 mA g^{-1}. The intrinsic defects of NSGs provided enhanced active sites to the composite electrode and improved the electrochemical performance.

6.1.5. PDCs in sodium-ion batteries

Compared to LIBs, SIBs are advantageous because they have less fabrication cost, they require less toxic electrolytes, and they provide grid-scale energy storage opportunity.[158] However, the large size of the Na ion (1.02 Å), sluggish kinetics, and undesirable volume changes limit the choice of suitable electrodes in SIBs. Although PDCs have been used in recent studies to evaluate their electrochemical performance in SIBs, they are less frequently utilized than LIBs.

Kaspar et al. introduced the SiOC/hard carbon composite anode in SIBs.[159] Glucose was used as a hard carbon source, and SiOC was derived from polysiloxanes mixed with a wt. ratio of 10.5:1. The as-synthesized SiOC/HC composite anode delivered a specific capacity of 201 mAh g^{-1} with coulombic efficiency of 65%. The microporous nature of the hard carbons enhanced the electrochemical performance of SiOC in the SIBs. Lee et al. integrated Sb into SiOC to fabricate a composite anode for SIBs.[160] Antimony acetates were dispersed in silicone oil and then pyrolyzed at 900 °C to synthesize the SiOC/Sb composite electrode. The composite electrode delivered a high first cycle capacity of 510 mAh g^{-1} at a current rate of 0.5C, and exhibited 453 mAh g^{-1} at a higher current rate of 20 C. Moreover, 97% of the initial capacity was retained after 250 cycles. The presence of a free C phase in the SiOC improved the electrochemical performance, and the homogenous distribution of Sb in the SiOC matrix provided structural stability.

Chandra et al. utilized silicone oil to synthesize SiOC anodes for SIBs.[161] The oil was pyrolyzed at 700°C , 800°C , and 900°C and then mechanically milled and pulverized. The sample pyrolyzed at 900 °C demonstrated the best results, delivering a specific capacity of 160 mAh g^{-1} at a current density of 25 mA g^{-1} after 200 cycles. In addition, the SiOC electrode showed an

excellent cycling stability with only 0.09 mAh g^{-1} capacity decay per cycle after 650 cycles. The large amount of free carbon was essential for good capacity of the SiOC electrodes in SIBs.

Soares et al. utilized SiOC to functionalize MoS_2 to improve electrode stability in SIBs.[162] SiOC precursor was added to MoS_2 in a 1:1 weight ratio, and then heated at 800 °C to achieve a SiOC/MoS_2 composite. The introduction of SiOC with MoS_2 prevented the dissolution of MoS_2 into the electrolyte and improved the cycling stability of the electrode. The SiOC/MoS_2 anode exhibited an 86.5% capacity retention over 100 cycles at a current density of 200 mA g^{-1}. The composite electrode also showed a specific capacity of 226.1 mAh g^{-1} at a current density of 25 mA g^{-1}.

Putra et al. studied a SiOC/graphene composite anode for SIBs.[163] They investigated the effect of fluorinated ethylene carbonate (FEC) in a propylene carbonate (PC) electrolyte. The addition of FEC to the electrolyte improved the specific capacity from 126 mAh g^{-1} to 198 mAh g^{-1}, at a current density of 50 mA g^{-1} due to the higher diffusion coefficient (1.73×10^{-16} cm^2 s^{-1}) of Na ions in the SiOC anode with the FEC additive electrolyte. Table 1 summarizes some of the important results of PDC anodes in LIB and SIBs.

Table 1 Electrochemical performance of PDC nanocomposites as anodes in LIBs and SIBs.

Sample	Pyrolysis Temperature (°C)	Current Density (mA g^{-1})	First Cycle Reversible Capacity (mAh g^{-1})	Reversible Capacity (mAh g^{-1}) (After *N* cycles)	Reference
SiOC microbeads	1000	360	858	805 (300)	141
SiOC aerogel	900	360	763	570 (50)	142
SiCN powder	1000	40	900	826 (100)	127
SiOC/graphite	1000	500	458	450 (400)	130

SiCNO/graphene oxide	1000	400	530	~500 (350)	143
SiOC/CNT	1000	100	948	846 (40)	144
Si(B)CN/CNT	1100	100	362	412 (30)	145
Si(Al)CN/CNT	1000	100	577	540 (50)	132
SiCN/BN	1000	100	517	449 (40)	146
Si(B)CN/graphene	1000	450	~790	785 (800)	134
SiOC/TiO_2	800	208	725	-	147
SiOC/MnO	-	100	760	770 (200)	133
SiOC [a]	900	25	189	160 (200)	138
SiOC/Sb [a]	900	0.2 C	~407	344 (150)	148
SiOC/graphene oxide[a]	900	20	233	226 (20)	140

[a] SIB systems.

6.2. Outlook

Overall, Si-based PDC systems are unique compounds that offer wide range of compositions, tunable physical properties and adaptive fabrication techniques. Traditionally studied as ultrahigh temperature materials for aerospace applications, PDCs have emerged as promising electrochemical energy storage materials in the past decade. High energy density, long-term cycling stability, and superior rate capability render PDCs-based electrodes beneficial over traditional hard carbon-based electrodes in metal-ion rechargeable batteries. Specifically, negligible capacity fading for certain C-rich PDCs at higher current in LIBs, and relatively stable cycling of large Na ions in the amorphous PDC structure for SIBs are major advantages over traditional graphite electrode. Nonetheless, shortcomings in using PDC anodes such as relatively high processing cost, voltage hysteresis or energy inefficiency during electrode charging, and first-

cycle capacity loss have hindered commercialization of PDC electrodes in batteries. Recent literature shows that minimizing particle size or utilizing PDC/nanomaterials composites as active electrodes may further improve storage capacity and improve diffusion of ionic species which may lower the voltage hysteresis. A greater control over composition of various phase (SiC, SiO_2, C-C) during the processing of PDCs, as well as *in-situ* monitoring of the electrode/electrolyte interface of PDC electrodes will be key to effective utilization of PDCs in energy storage devices.

7. Advanced Characterization

As in any ceramic system, control over resulting microstructure in functional PDC nanocomposites is imperative for reproducibility through processing as well as optimization of target functional properties. To achieve such control, rigorous, cross-correlative characterization is necessary through each processing step—not only monitoring the complex evolution of the polymer matrix, but also its interactions with nanoparticle filler and the structural influences of different processing conditions. With so many structural knobs to turn, discernment of nano- and microstructural changes throughout processing has been and still is a developing topic of interest in the PDC community. In this section, we will outline characterization techniques for *ex-situ* microstructure discernment post-pyrolysis, advanced characterization including *in-situ* techniques that have been or could be applied to this complex system for increased understanding. In each case, we will present a study where such techniques have successfully uncovered an aspect of the structure of functional PDC nanocomposites.

7.1. *Ex-situ* techniques for determining microstructure during processing.

During PDC processing, the major transition occurs from amorphous, cross-linked polymer to ceramic material. Here the PCP undergoes dramatic volume shrinkage and densification owed

to organic gas evolution, removing most of the organic carbon content within the matrix. Some free carbon remains in the structure along with a phase separated Si-rich region for Si-based PDCs such as SiCN, SiC, and SiOC.[35,172,173] For SiC, Si-rich regions include amorphous networks of SiC_4 and SiC_xO_{x-4} tetrahedra, Si-C-C-Si, and Si-C-C-H.[172] For SiOC, the amorphous Si-rich regions are similar though contain much more oxygen bonding within silicon tetrahedra: SiC_4, SiC_3O, SiC_2O_2, $SiCO_3$, and SiO_4.[35] As pyrolysis temperatures increase, structural changes occur within all domains until reaching elevated temperatures around 1200-1300ºC, where a transition from amorphous to crystalline begins through distinct-phase nanodomain formation of SiC and graphitic carbon.[172,174] The extent and onset of this crystalline shift depends on the species and amount of free carbon formation throughout pyrolysis, as free carbon is known to increase the matrix's resistance to crystallinity.[173] Resulting structure has been shown to rely heavily on starting precursors such as PCP backbone structure and functional groups,[175] transition metal additives as filler,[176] and processing conditions such as ramp rate, temperature, and gas flow.[3] Achieving target properties rely heavily on control over nano- and microstructures, so careful consideration of carbon evolution, silicon-bonding, and phase transformation is necessary. This has often been achieved through a host of *ex-situ* spectroscopies, X-ray scattering techniques, microscopy techniques, and thermal analyses, which we highlight in the following text.

7.1.1. Spectroscopies (FTIR, NMR, Raman)

Fourier transform infrared (FTIR), nuclear magnetic resonance (NMR), and Raman spectroscopies are often used to probe molecular bonding and chemical moieties in both amorphous and crystalline networks. In each case, electromagnetic radiation interacts with a material's bonds to form a spectral fingerprint.

FTIR: In FTIR, incident infrared radiation and absorbance (or percent transmission through the sample) is monitored. Incident radiation can be absorbed by the sample and induce vibrational modes of polar bonds. A detector collects the radiation transmitted through the sample and forms a fingerprint of missing energies where sample absorbance has occurred at characteristic energy levels, revealing identity of bonds in the sample. For polar FTIR-active bonds, stronger bonds (triple vs double vs single) vibrate at higher frequency and therefore higher energy. Bonds involving heavier atoms, however, vibrate at lower frequency following Hooke's Law. The concentration of polar molecules in a sample is related to FTIR absorbance following Beer's Law. The more polar a bond, the higher the higher the amplitude of stretching frequency relative to other, less polar bonds.[177] Nonpolar, symmetric bonds are not visible in FTIR spectroscopy.

FTIR is often used in polymer and nanostructured systems to monitor crosslinking or ligand bonding on a metal surface. This makes this method valuable for PDC systems, even at lower processing temperatures prior to pyrolysis. One such experiment with a polysiloxane PCP monitors the extent of polymer crosslinking while varying loadings of metal centers within the matrix. In Martin et al., two polysiloxanes are mixed with Ti- and Zn-salts in an effort to induce PCP crosslinking. Polymer crosslinking for this system is trackable by comparing the FTIR signal contributions from the free polymer and the blue-shifted, coordinated polymer at the ligand coordination site, indicating polymer anchorage to the metal center.[23] The findings in this study emphasize the power of FTIR in determining crosslinking during the non-crystalline lifetime for PDC processing.

NMR: In NMR, the sample is held under a constant magnetic field then exposed with radio frequency (RF) of different wavelengths to produce a spectrum. The net electromagnetic field of nuclei with odd number of protons and/or neutrons will align perfectly with or against the direction

of the applied magnetic field into alpha and beta spins, respectively. These spins will then be excited to become resonant (flipping back and forth between alpha and beta spins states) when interacting with specific RF. The RF required to induce resonance between spin states depends on the energy split between alpha and beta spin states, which is characteristic to the identity of the nucleus and is influenced by bonding environment. NMR gives a detailed picture of local structure between certain sets of molecules but is limited to the specific nuclei that can be detected by this method. For PDCs, NMR becomes interesting to understand molecular moieties that appear in the amorphous matrix post-pyrolysis, non-crystalline and therefore undetectable by lab XRD. In the case of polysiloxane precursors later forming SiOC ceramics, ^{29}Si and ^{13}C NMR have been used in concert to understand and detect the composition of Si-O-C tetrahedra that form, the surrounding amorphous sp^2 hybridized C network, and even the distance separating the tetrahedra.[178,179]

Raman: In contrast to FTIR, the bonds probed in Raman spectroscopy are nonpolar and symmetric. Raman-active molecules must exhibit an induced change in their polarizability whether through a difference in size, shape, or orientation of electron cloud. Through this method, symmetric stretches and vibrations between bonds are tracked through inelastic energy transfer while the sample is irradiated by visible light of varying frequency. Some of the incident light is absorbed by the sample through molecular vibrations, causing a small amount to be reemitted at lower energy.

Raman is particularly useful for understanding the structural characteristics of free carbon that remain in the PDC matrix despite reaching high temperatures. A previous study has used Raman to understand the structure of free carbon in an SiC PDC post-pyrolysis at high processing temperatures.[172] In this study, Wang et al. tracks the major D and G bands corresponding to free carbon and the minor D', D", and I bands corresponding to disordered graphite, amorphous carbon,

and sp^3 C—C bonds, respectively. Careful analysis of the G band position and full width half max (FWHM) through changing temperatures (1000ºC -1400ºC) gave an observable phase transfer from amorphous C-content to crystalline at these elevated temperatures, indicated by an increased Raman shift and decreased FWHM.[172] The amount and structure of free carbon remaining in the PDC matrix has been found to majorly influence the crystallization thermodynamics and kinetics, so the ability to monitor its formation and evolution through Raman spectroscopy is powerful.

7.1.2. X-ray Scattering (XRD, SAXS, PDF)

XRD: When X-rays interact with matter, several interactions are possible, though scattering is the focus of this subsection. Diffraction is one result of scattering that occurs when several atoms scatter a beam of X-rays and cooperate to form constructive interference. The conditions by which a diffracted, coherently scattered beam forms are succinctly summarized by Bragg's Law which relates structural and compositional parameters (d-spacing) to source wavelength (λ) and diffracted beam exit angle (θ) (Eqn. 1). However, Bragg scattering relies on two assumptions: the matter is a perfect, infinite crystal lattice, and the X-ray beam is perfectly parallel and monochromatic.

$$n\lambda = 2dsin\theta \quad (1)$$

The perfect periodicity of the lattice is essential to this relationship, as periodicity allows strong constructive interference for a few angles and perfect cancellation in all others owed to destructive interference.[180]

For the PDC system, the Bragg assumption of infinite periodicity and crystallinity does not hold until high processing temperatures when crystalline domains begin to form. These crystalline domains first appear as nano-domains within an amorphous matrix, and once at a certain size (~2-10 nm depending on X-ray source) become detectable through broadened Bragg peaks. The

broadening occurs because there are finite lattice planes in nano-domains, causing broadening due to imperfect destructive interference right around the Bragg angle. In addition to composition, nanodomain ripening can be monitored through XRD, as the Scherrer function provides an estimate of crystallite size (t) as it relates to peak broadening at FWHM (B) for a given Bragg angle (Eqn. 2).

$$t = \frac{0.9\lambda}{Bcos(\theta_B)} \quad (2)$$

SAXS: A more accurate understanding of nanodomain morphology can be achieved through small-angle X-ray scattering (SAXS). Similar to XRD, SAXS is a measure of coherent scattering though it happens at considerably smaller angles ($2\theta < 10°$). Small collection angles allow capture of colloid-sized (10 Å - 100 nm) structural features such as size, morphology, and scatterer volume based on differences in electron density within a solution.[181] Because SAXS measures differences in electron density within some medium, this technique has often been applied to nanoparticles in colloidal solutions. For PDCs, SAXS-trackable differences in electron density could arise from nanofiller dispersed in a PCP or PDC matrix, crystalline nanodomain formation during amorphous polymer to ceramic conversion, or through the formation of porosity within the PDC matrix.

Different regions of the SAXS pattern lend unique information about the sample. The Guinier region exists at low-q where the average particle dimension (known as the radius of gyration, R_g) can be extracted from the slope ($-R_g^2$) of a Guinier plot ($\ln(I)\ vs.\ q^2$).[181,182] Higher q-ranges give information on morphology and templating through Porod analysis, indicated by the fitted value for the Porod exponent (d), which determines morhpology.[181]

PDF: From XRD, one can get composition information and size estimates from crystalline domains in PDCs processed at high temperatures, but information on the amorphous component

cannot be gathered. Total scattering must be used to understand the amorphous polymer matrix and its local structure changes throughout processing. This, which is a combination of both Bragg and diffuse scattering components, lends information on average structure and local structure and can be collected from high-energy X-ray scattering. By performing a Fourier transform of total scattering data, a pair distribution function (PDF) is created in real space (Eqn. 3) which maps probabilistic bond distances in a histogram and builds a blueprint for local structure.[183] Due to their higher contributions to diffuse scattering signal, polymers and nanocomposites are excellent materials for PDF analysis, even at low processing temperatures where no long range order is apparent. Despite the promise of PDF for PDCs, very few systems have been probed using PDF.

$$\mathrm{G(r)} = \frac{2}{\pi}\int_0^\infty q(S(q)-1)\sin(qr)\,dq \tag{3}$$

7.1.3. Electron Microscopy (TEM, SEM, EDS)

In electron microscopy, a beam of high energy electrons is focused onto a sample plane containing some matter and a collection of scattering and absorbing events lead to structural, compositional, and morphological characterization. By utilizing electrons, resolution is vastly improved over optical microscopy due to resolution limitations with visible light and the low de Broglie wavelength of electrons.[184] Several electron microscopy techniques exist, however in this work we focus on transmission electron microscopy (TEM), Scanning Electron Microscopy (SEM), and a few specialized techniques that can be performed with each.

TEM: Transmission Electron Microscopy is a technique in which a fine, focused, monochromatic beam of electrons at high accelerating voltage is transmitted through a very thin piece of matter, giving a variety of interactions that yield structural and morphological information. By pushing resolution into sub-atomic region, high resolution TEM (HRTEM) can be performed and often show lattice fringes of the sample, lending structural information such as lattice spacing

and surface facet characterization. Beyond conventional imaging, electron diffraction can be performed on crystalline samples, providing structural information such as lattice parameters and d-spacing. Compositional analysis is also possible both quantitatively and qualitatively through electron energy loss spectroscopy (EELS) and energy dispersive X-ray spectroscopy (EDS). EELS and EDS are often performed together, as EELS works well for quantitative compositional analysis of lighter elements while EDS qualitatively maps heavier elements.

While TEM allows high resolution imaging, structural, and compositional analysis, it is limited by its need for incredibly thin samples. This becomes challenging for brittle ceramic material as samples must be reduced to fine powders prior to analysis.

SEM: Scanning Electron Microscopy is a technique where a beam of electrons rasters a sample to form an image of the surface topography and composition through detection of secondary electrons (SE) and back scattered electrons (BSE) that have interacted with matter. The beam of electrons is at a considerably lower accelerating voltage than in TEM, corresponding to a lower resolution though still much greater than that of optical microscopy. Rather than atomic level resolution giving structural lattice information, SEM resolution allows for size and morphological grain information. However, advantages of SEM include its ability to perform multiple analyses at once by use of multiple detectors, relative cheapness compared to TEM analysis, and ability to analyze thick samples which makes for easier sample preparation.

EDS: Energy dispersive X-ray spectroscopy is possible in either an SEM or TEM and provides valuable elemental mapping over an image. In the SEM, this is made possible just by insertion of a detector that will catch characteristic x-rays. These are emitted as a result of the beam exciting and ejecting core electrons and forcing valence electrons to decay down to the core shell, releasing an X-ray of characteristic energy depending on the element. For SEM, careful

consideration of beam accelerating voltage is necessary as it must be high enough to excite the core electrons in the sample for each known element. For TEM, insertion of an EDS detector is also necessary, but the microscope must also be taken into Scanning TEM (STEM) mode, where the beam is focused down to a nanoprobe and exposed to the surface of the sample in one fine location. In each scope, EDS allows for elemental mapping which has high implications for PDC processing since Si-rich and C-rich regions are known to form, even forming free carbon crystalline domains at high enough temperatures. Though commonly used as a qualitative technique to visually observe elemental contributions between grains in a sample, quantitative information can also be extracted if intensive calibration is performed. EDS is most effective for heavier elements such as transition metals and beyond. Though still possible with lighter elements such as carbon and oxygen, accurate EDS signals from lighter elements can be challenging to acquire. Careful alignment and optimization of counts is necessary to get a trustworthy qualitative map.

7.1.4. Thermal Gravimetric Analysis and Differential Scanning Calorimetry

A considerable percentage of mass loss occurs throughout processing of PDC materials owed to the large organic component comprising the starting polymers. As such, strategies to improve mass loss have been developed including the utilization of catalysts or metal ions in the PCP to induce early crosslinking and improve ceramic yield.[23,117] In these efforts, thermal gravimetric analysis (TGA) is employed to monitor mass loss through each stage of processing. TGA simply heats a known mass of sample and monitors the mass throughout the heating profile.

Though simple, TGA can lend itself to the PDC community in several ways. This is included in probing graft density of PCP-grafted nanofillers prior to dispersion into the PCP matrix, as highlighted in previous works to monitor effects of graft density on dispersion versus

aggregation.[185–187] Additionally, TGA-mass spectroscopy offers the ability to monitor the species of organic component lost through pyrolysis, found as methane and hydrogen evolution for SiOC in 2013.[188] In the same study, the rate of mass lost was related to the overall rate of the processing steps for PDC materials, shedding light on reaction kinetics for this class of materials.

A complimentary technique to TGA is Differential Scanning Calorimetry (DSC), which monitors the amount of heat required to change the temperature of the sample. This becomes useful to gauge the endothermic/exothermic nature of certain transitions, reactions, or structural changes in the system. Specific to PDC processing, DSC could be used to track matrix changes from amorphous to crystalline, or reactions at the interface of dispersed nanofillers such as oxidation or formation of intermetallic species.

7.2. Advanced Techniques

Despite the host of characterization techniques that have been applied to understanding the structural changes occurring on the micro- and nanoscale of PDCs throughout processing steps, several questions remain. In particular, local structure evolutions have largely not been probed which could lend information on the unexplored and misunderstood amorphous-crystalline ceramic transition occurring at high temperatures. In this section, we highlight some advanced characterization techniques which have been or could be used to better understand these changes during processing.

7.2.1. *In-situ* high energy XRD to monitor particle-matrix interactions

Using a high energy synchrotron source paired with a cryo-stream or resistively heated flow cell, *in-situ* high energy XRD or PDF is possible through processing steps for PCP during conversion from polymer to ceramic. Due to fast acquisition capabilities for XRD, one could probe changing average structure through the entire heating profile. From this, a profile of amorphous-

to-crystalline signal can be monitored with the emergence of sharp peaks indicating crystallinity. For a PDC system with added nanofillers, potential particle ripening or oxidation with increasing processing temperature can also be tracked, depending on the size of nanofiller.

Though PDF has longer acquisition time compared to XRD, it is still considered fairly rapid (~3-5 minutes) when performed at a dedicated beamline and offers potential to paint a detailed picture of local structure information from beginning polymeric structure, to crosslinked polymer, to amorphous ceramic, and finally crystallized ceramic. Though challenging, using PDF to decipher PCP structure prior to any processing could be possible, as demonstrated by Terban et al. in a PDF study of an unoriented polyamide polymer species.[189] Crosslinking is the first stage of processing and will be apparent through PDF with the emergence of some long range structure and a few added peaks in the low-r region of in the G(r) signal. In terms of the amorphous polymer to crystalline ceramic transition, the local structure evolution has remained mysterious though seems to evolve through Si-rich and C-rich domains within the structure, including Si-O-C tetrahedra formation in the Si-rich region.[35] From PDF, a detailed bond-by-bond map could elucidate this ambiguous transition.

In addition to understanding matrix structure, PDF could also effectively monitor surface evolution of nanofiller while in the matrix through high processing temperatures. Another study has monitored surface nanoparticle interactions with solvent through differential PDF, a technique where solvent structure factor signal is subtracted from nanoparticle in solvent structure factor in order to isolate particle and particle-solvent interactions in the *G(r)* signal.[190] Following similar methodology, one could isolate particle matrix interactions occurring at high processing temperatures including possible formation of intermetallics, heterogeneous nucleation of carbon, surface oxidation, or Ostwald ripening.

7.2.2. *In-situ* SAXS to uncover microporosity evolution

Attempts to monitor porosity in PDCs have often utilized TEM, STEM, and *ex-situ* SAXS. This has been successful in many cases, however, monitoring the exact stable formation and later destruction owed to densification at high temperatures becomes challenging. This is due to the highly sensitive nature of the pores with respect to the processing atmosphere and the extremely small size of some pores throughout evolution. Once the sample is removed from its pyrolysis conditions (temperature, atmosphere) oxidation and pore evolution causes changes to the pores giving an inaccurate picture of the evolution occurring throughout processing exclusively. In 2021, Konegger et al. answered these concerns by releasing a study on a novel *in-situ* SAXS set up that allows for measurement up to 900ºC. In this experiment, crosslinked polysilazane samples are heated under two unique atmospheres and scans are taken every 50ºC to monitor changes in electron density as they relate to microporosity within the polymer through processing.[191] Changes in electron density at these high temperatures, owing to pore formation and later collapse, allow trackable temperature of onset pore formation, pore size ripening or narrowing, increase in number of pores of similar size, and temperature of pore degradation and densification.[191] This study has large implications for trackable pore information during the polymer-to-ceramic conversion with the possibility to compare effects from different pyrolysis conditions such as gas flow. While this study is for one unique PDC system, the promise of *in-situ* SAXS through pyrolysis is vast as PDC systems are becoming more tailored with inclusion of functional nanofillers or uniquely functionalized PCP backbones.

7.2.3. X-ray probed laser annealed mapping (XPLAM)

The transition from amorphous polymer to crystalline ceramic, as mentioned, is largely not well understood for the PDC system. Because of the sensitivity of these domain formations to

various processing conditions, isolating the rate, mechanism, and influence of each processing condition for these structural transitions is challenging. To answer these questions, detailed characterization probing phase transformation is necessary.

A promising candidate to gauge the transformations occurring in PDCs over varying processing conditions is a technique which combines laser spike annealing (LSA) with synchrotron X-ray diffraction to spatially map phase formation over varying temperatures, penned as X-ray probed laser anneal mapping (XPLAM) and reported in 2021 by Bell et al.[192] LSA is a technique which utilizes a Gaussian-shaped laser to rapidly heat a sample by scanning laterally across the surface. The Gaussian laser shape allows an invariant temperature over the lateral scan direction paired with a controlled temperature gradient orthogonal to the scan direction. By pairing this technique with synchrotron XRD, Bell et al. monitors the transitions from amorphous Bi_2O_3 to cubic, tetragonal, and monoclinic phases based on varied processing temperature, dwell time, and quench rate. These phases are spatially mapped on the sample as they correspond to the different processing conditions by focusing the X-ray beam spot to a size similar to the LSA probe and performing XRD both laterally and orthogonally.[192] For the Bi_2O_3 system, XPLAM allowed both the creation of a temperature-dwell-transformation (TDT) diagram and direct thermodynamic and kinetic measurements of the phase transformations, made trackable by phase nucleation and growth observation via domain size ripening using the Scherrer function.[192]

Though it has not yet been applied to the PDC system, XPLAM could prove invaluable to further understand PDC processing as one rapid anneal produces a variety of processing conditions over a sample surface in turn producing several trackable phase changes as they correspond to the varied heating conditions. With heating capabilities up to 1400°C, XPLAM is a logistically viable

characterization technique that holds promise to significantly impact the current picture of PDC structural evolutions throughout processing.

7.2.4. 4D-STEM

For many of the common techniques mentioned in the first subsection, the co-analysis of both amorphous and crystalline matter in PDC materials is not trivial. Spatial resolution at size scales required for PDC nanocomposites throughout processing is also lacking for many of these common techniques. To achieve spatial resolution for a matrix of mixed amorphous and crystalline content, advanced characterization is necessary.

4D-STEM is a complex microscopy technique that gives promise to fill these gaps for PDCs. The nanoprobe mode in STEM allows single data points to be gathered at the beam's point of contact with the matter, whether it be EDS, EELS, or electron diffraction. In 4D-STEM, the nanoprobe is rastered over a 2D array of pixels, generating EDS, EELS, or electron diffraction patterns at each pixel probe position.[193] The result is a 4D data cube, consisting of a 2D image with a 2D pattern or spectra collected at each pixel. The collection of such a large and detailed set of data has recently been made possible through detector advancements allowing for high speed and efficient data collection and through the availability of vast computational power required for this technique.[193] Implications of this technique include the ability to produce phase contrast images at high resolution as well as an understanding of crystalline and semicrystalline structure and orientation mapping within the image,[193] particularly useful for the PDC system.

Yang et al. has put 4D-STEM to the test in the post-processing analysis of a commercial polysiloxane turned SiOC PDC material. [194] Yang et al. employs 4D-STEM to effectively map the emergence of 3-4 nm turbostratic carbon nano-formations on SiC and SiO_2 domains over a 100 nm x 100 nm grid of O- and C-rich amorphous regions of the SiOC ceramic. Diffraction patterns

were collected at each pixel over the imaged 2D grid, followed by Fourier transform to give the radial distribution function (RDF) at each probe location.[194] The extraction of RDF gives spatial information through real-space atom by atom distances within the matrix, including information form both crystalline and amorphous components (similar to information gained from PDF). The SiOC local structure can then be mapped by pixel on a 100 x 100 nm grid in a resolution of 1-2 nm.[194] The value that 4D-STEM can add to the PDC community is represented by the key findings in this SiOC study: more likely formation of sp^2 C in C-rich SiC_xO_{4-x} regions than in O-rich regions, heterogeneous nucleation of free carbon on SiC and SiO_2 clusters, and evidence that the turbostratic carbon layer acts as a diffusion barrier to SiC and SiO_2 domain ripening.[194] So far, 4D-STEM has only been used for one commercial SiOC system. Moving forward, utilization of 4D-STEM on more tailored PDC nanocomposites will unearth more structure-processing-property relations and provide valuable information on functional PDC systems, including information on in the influence of added nanofiller to the resulting structure.

7.3 Outlook

Well-developed *ex-situ* techniques in PDC characterization have done much to elucidate the fact that structural transitions are complex during PCP processing, even for the most simplistic and commercial systems. Moving forward, PDCs offer rich promise as high temperature, functional nanocomposites for highly tailored applications. To optimize properties and therefore PDC functionality, a full picture of structure-processing-property relations is imperative. This will only be achievable through the development of advanced characterization techniques and their application to several PDC systems. Gaps to fill include techniques that allow information on local structure evolution, co-analysis of amorphous and ceramic components, and high-resolution spatial mapping of phases formed at different processing conditions.

8. Summary and Outlook

From molecular precursor design to advanced characterization of PDCs, we can probe how molecular design and processing conditions will correlate to controlled functional properties for enhanced LEO erosion resistance, electrical conductivity, magnetism, gas diffusion, and charge storage. Such controlled functionalities enable applications in gas-to-liquid fuel production, secondary batteries, gas separation, hydrogen storage, and scramjet-based hypersonic vehicles. We need to quantify phase distribution and composition of final ceramic nanocomposites to engineer these materials for end use applications. Incorporation of transition metal centers in PDCs can decrease processing temperatures for nucleating free carbon to increase electrical conductivity. Increased electrical conductivity has potential for increasing electrocatalytic activity due to increased charge carrier transport kinetics and Li-ion and Na-ion charge storage. Porosity controls gas flow in heterogeneous catalysis support and mechanisms of Na ion charge storage. Thus, future work in designing and constructing complex porous structure of PDCs will enable the tuning of catalytic activity, selectivity, high-rate capability, or capacity. Future work should also build upon the extensive body of work on porogen interactions with ceramic matrices to investigate the role of anisotropic pores as well as hierarchical and graded pore structures for controlling reaction and gas flow kinetics. The structure-property-performance relations of PDCs rely on understanding local structure evolution during performance. Future work on *ex-situ* characterization of as-prepared PDCs will enable rational design of materials. Furthermore, the cross-correlation of multiple advanced characterization techniques will be required to resolve atomic structure solutions necessary for understanding local structure evolution during service. For energy storage applications such as Li-ion and Na-ion batteries, designing electrochemical cells capable of

operando dual modes of characterization (i.e. scattering and spectroscopy)[195] will be key for mechanistic insight structural and morphological changes during cycling. Similarly, high-temperature reaction cells will enable *in-situ* mapping of microstructural changes during catalysis.

Author Declarations

Conflict of Interest

The authors have no conflicts to disclose.

Acknowledgements

PL and VDN gratefully acknowledge support from the Air Force Research Lab (AFRL) Defense Associated Graduate Student Innovators (DAGSI) Award No. RX21-OSU-20-2 and AFSOR Young Investigator Program (YIP) Award FA9550-22-1-0074. GS and SBM's work on PDCs is supported through National Science Foundation (NSF) grant number 1743701. KL gratefully acknowledges support from the National Science Foundation under grant number CBET-2024546.

References

[1] Z. Ren, S. Bin Mujib, and G. Singh, Materials (Basel). **14**, 1 (2021).

[2] A. Xia, J. Yin, X. Chen, X. Liu, and Z. Huang, Crystals **10**, (2020).

[3] E. Barrios and L. Zhai, Mol. Syst. Des. Eng. **5**, 1606 (2020).

[4] G. Mera, M. Gallei, S. Bernard, and E. Ionescu, Nanomaterials **5**, 468 (2015).

[5] D.E. Glass, 15th AIAA Int. Sp. Planes Hypersonic Syst. Technol. Conf. 1 (2008).

[6] R. Sujith, S. Jothi, A. Zimmermann, F. Aldinger, and R. Kumar, Int. Mater. Rev. 1 (2020).

[7] E. Bernardo, P. Colombo, and S. Hampshire, J. Eur. Ceram. Soc. **29**, 843 (2009).

[8] A. Viard, D. Fonblanc, D. Lopez-Ferber, M. Schmidt, A. Lale, C. Durif, M. Balestrat, F. Rossignol, M. Weinmann, R. Riedel, and S. Bernard, Adv. Eng. Mater. **20**, 1 (2018).

[9] E. Ionescu, S. Bernard, R. Lucas, P. Kroll, S. Ushakov, A. Navrotsky, and R. Riedel, Adv. Eng. Mater. **1900269**, 1 (2019).

[10] K.J. Kim, J.H. Eom, T.Y. Koh, Y.W. Kim, and W.S. Seo, J. Eur. Ceram. Soc. **36**, 2705 (2016).

[11] K. Lu, D. Erb, and M. Liu, J. Mater. Chem. C **4**, 1829 (2016).

[12] P. Furtat, M. Lenz-Leite, E. Ionescu, R.A.F. MacHado, and G. Motz, J. Mater. Chem. A **5**, 25509 (2017).

[13] C. Shen, J.E. Calderon, E. Barrios, M. Soliman, A. Khater, A. Jeyaranjan, L. Tetard, A. Gordon, S. Seal, and L. Zhai, J. Mater. Chem. C **5**, 11708 (2017).

[14] P. Moni, M. Wilhelm, and K. Rezwan, RSC Adv. **7**, 37559 (2017).

[15] Y. Bolbukh, K. Terpiłowski, R. Kozakevych, D. Sternik, A. Deryło-Marczewska, and V. Tertykh, Nanoscale Res. Lett. **11**, (2016).

[16] K.L. Martin, D.P. Street, and M.B. Dickerson, Chem. Mater. **32**, 3990 (2020).

[17] M. Seifert, P. Gonçalves, T. Justus, N. Martins, A.N. Klein, and G. Motz, Mater. Des. **89**, 893 (2016).

[18] C. Luo, W. Duan, X. Yin, and J. Kong, J. Phys. Chem. C **120**, 18721 (2016).

[19] S.C. Zunjarrao, P. Dyjak, A. Rahman, J.D. Metzger, and R.P. Singh, J. Am. Ceram. Soc. **99**, 2260 (2016).

[20] W. Duan, X. Yin, C. Luo, J. Kong, F. Ye, and H. Pan, J. Eur. Ceram. Soc. **37**, 2021 (2017).

[21] X. Wang, F. Schmidt, D. Hanaor, P.H. Kamm, S. Li, and A. Gurlo, Addit. Manuf. **27**, 80 (2019).

[22] P. Colombo, J. Schmidt, G. Franchin, A. Zocca, and J. Günster, Am. Ceram. Soc. Bull. **96**, 16

(2017).

[23] K.L. Martin, M.J.S. Parvulescu, T.A. Patel, P. Mogilevsky, T.S. Key, C.M. Thompson, and M.B. Dickerson, J. Eur. Ceram. Soc. (2021).

[24] H. Ichikawa, Annu. Rev. Mater. Res. **46**, 335 (2016).

[25] P. Jana, E. Zera, and G.D. Sorarù, Mater. Des. **116**, 278 (2017).

[26] A. Lale, A. Wasan, R. Kumar, P. Miele, U.B. Demirci, and S. Bernard, Int. J. Hydrogen Energy **41**, 15477 (2016).

[27] P.M. Rewatkar, T. Taghvaee, A.M. Saeed, S. Donthula, C. Mandal, N. Chandrasekaran, T. Leventis, T.K. Shruthi, C. Sotiriou-Leventis, and N. Leventis, Chem. Mater. **30**, 1635 (2018).

[28] M. Biesuz, E. Zera, M. Tomasi, P. Jana, O. Ersen, W. Baaziz, A. Lindemann, and G.D. Sorarù, Appl. Mater. Today **20**, 100648 (2020).

[29] F. Thévenot, C. Doche, H. Mongeot, F. Guilhon, P. Miele, and B. Bonnetot, J. Eur. Ceram. Soc. **17**, 1911 (1997).

[30] P.J. Fazen, J.S. Beck, A.T. Lynch, E.E. Remsen, and L.G. Sneddon, Chem. Mater. **2**, 96 (1990).

[31] L.G. Sneddon, M.G.L. Mirabelli, A.T. Lynch, P.J. Fazen, K. Su, and J.S. Beck, Pure Appl. Chem. **63**, 407 (1991).

[32] K. Su, E.E. Remsen, G.A. Zank, and L.G. Sneddon, Chem. Mater. **5**, 547 (1993).

[33] B. Bonnetot, H. Mongeota, D. Cornu, P. Miele, and C. Bernard, J. Mater. Chem. **9**, 757 (1999).

[34] D. Cornu, P. Miele, B. Toury, B. Bonnetot, H. Mongeot, and J. Bouix, J. Mater. Chem. **9**, 2605 (1999).

[35] K. Lu and D. Erb, Int. Mater. Rev. **63**, 139 (2018).

[36] G. Mera, M. Gallei, S. Bernard, and E. Ionescu, Nanomaterials **5**, 468 (2015).

[37] M. Narisawa, Materials (Basel). **3**, 3518 (2010).

[38] Q. Wen, Z. Yu, and R. Riedel, Prog. Mater. Sci. **109**, 100623 (2020).

[39] R. Bhandavat, M. Cologna, and G. Singh, Nanomater. Energy **1**, 57 (2012).

[40] Z.Y. Hu and Q.S. Ma, Cailiao Gongcheng-Journal Mater. Eng. **47**, 19 (2019).

[41] T.C.D.E. Silva, V.F. Kettermann, C. Pereira, M. Simoes, M. Wilhelm, and K. Rezwan, J. Mater. Sci. **54**, 6471 (2019).

[42] S. Modena, G.D. Sorarù, Y. Blum, and R. Raj, J. Am. Ceram. Soc. **88**, 339 (2005).

[43] C. Downloads, *Polymer-Derived Ceramics and Their Space Cite as Living Reference Work Entry Latest Version* (2020).

[44] E.A. Davis and N.F. Mott, Philos. Mag. A J. Theor. Exp. Appl. Phys. **22**, 903 (1970).

[45] C. Godet, Philos. Mag. B **81**, 205 (2001).

[46] N.F. Mott, Philos. Mag. A J. Theor. Exp. Appl. Phys. **19**, 835 (1969).

[47] G. Lazar, K. Zellama, M. Clin, and C. Godet, Appl. Phys. Lett. **85**, 6176 (2004).

[48] J. Cordelair and P. Greil, J. Eur. Ceram. Soc. **20**, 1947 (2000).

[49] L.X. Wang, K. Lu, and R.X. Ma, Appl. Phys. a-Materials Sci. Process. **125**, (2019).

[50] E. Asenath-Smith, J.M. Noble, R. Hovden, A.M. Uhl, A. DiCorato, Y.-Y. Kim, A.N. Kulak, F.C. Meldrum, L.F. Kourkoutis, and L.A. Estroff, Chem. Mater. **29**, 555 (2017).

[51] K. Lu, D. Erb, and M. Liu, J. Mater. Sci. **51**, 10166 (2016).

[52] M. Fides, P. Hvizdoš, R. Bystrický, A. Kovalčíková, R. Sedlák, J. Sedláček, and R. Džunda, J. Eur. Ceram. Soc. **37**, 4315 (2017).

[53] Q. Wen, Z. Yu, Y. Xu, Y. Lu, C. Fasel, K. Morita, O. Guillon, G. Buntkowsky, E. Ionescu, and R. Riedel, J. Mater. Chem. C **6**, 855 (2018).

[54] B. Román-Manso, F.M. Figueiredo, B. Achiaga, R. Barea, D. Pérez-Coll, A. Morelos-Gómez, M. Terrones, M.I. Osendi, M. Belmonte, and P. Miranzo, Carbon N. Y. **100**, 318 (2016).

[55] C.G. Pantano, A.K. Singh, and H. Zhang, J. Sol-Gel Sci. Technol. **14**, 7 (1999).

[56](n.d.).

[57] J. Cordelair and P. Greil, J. Am. Ceram. Soc. **84**, 2256 (2004).

[58] P. Vallachira Warriam Sasikumar, E. Müller, P. Clement, J. Jang, E. Kakkava, G. Panusa, D. Psaltis, K. Maniura-Weber, M. Rottmar, J. Brugger, and G. Blugan, ACS Appl. Mater. Interfaces **12**, 17244 (2020).

[59] N. Yang and K. Lu, J. Eur. Ceram. Soc. **39**, 4029 (2019).

[60] J.Q. Zheng and K. Lu, J. Am. Ceram. Soc. **104**, 2460 (2021).

[61] N. Yang, M. Gao, J. Li, and K. Lu, J. Am. Ceram. Soc. **103**, 145 (2020).

[62] M.S. Cao, Y.Z. Cai, P. He, J.C. Shu, W.Q. Cao, and J. Yuan, Chem. Eng. J. **359**, 1265 (2019).

[63] C.J. Zhang, B. Anasori, A. Seral-Ascaso, S.H. Park, N. McEvoy, A. Shmeliov, G.S. Duesberg, J.N. Coleman, Y. Gogotsi, and V. Nicolosi, Adv. Mater. **29**, (2017).

[64] A.D. Dillon, M.J. Ghidiu, A.L. Krick, J. Griggs, S.J. May, Y. Gogotsi, M.W. Barsoum, and A.T. Fafarman, Adv. Funct. Mater. **26**, 4162 (2016).

[65] J. Gangadhar, A. Maheshwari, R.K. Bordia, C.N.S. Kumar, C. Kubel, and R. Sujith, Ceram. Int. **46**, 28156 (2020).

[66] A. Maheshwari, E.P. Gopikrishnan, J. Gangadhar, and R. Sujith, Mater. Chem. Phys. **239**, 121963 (2020).

[67] P. Moni, A. Deschamps, D. Schumacher, K. Rezwan, and M. Wilhelm, J. Colloid Interface Sci. **577**, 494 (2020).

[68] P. Moni, M. Wilhelm, and K. Rezwana, Rsc Adv. **7**, 37559 (2017).

[69] L.T. Lu, N.T. Dung, L.D. Tung, C.T. Thanh, O.K. Quy, N. V Chuc, S. Maenosono, and N.T.K. Thanh, Nanoscale **7**, 19596 (2015).

[70] A. Idesaki and P. Colombo, Adv. Eng. Mater. **14**, 1116 (2012).

[71] E.C. Stoner and E.P. Wohlfarth, Philos. Trans. R. Soc. London. Ser. A, Math. Phys. Sci. **240**, 599 (1948).

[72] M. Hojamberdiev, R.M. Prasad, C. Fasel, R. Riedel, and E. Ionescu, J. Eur. Ceram. Soc. **33**, 2465 (2013).

[73] L. Biasetto, A. Francis, P. Palade, G. Principi, and P. Colombo, J. Mater. Sci. **43**, 4119 (2008).

[74] Y. Zhao, T. Ling, S. Chen, B. Jin, A. Vasileff, Y. Jiao, L. Song, J. Luo, and S.Z. Qiao, Angew. Chemie - Int. Ed. **58**, 12252 (2019).

[75] K. Qi, X. Cui, L. Gu, S. Yu, X. Fan, M. Luo, S. Xu, N. Li, L. Zheng, Q. Zhang, J. Ma, Y. Gong, F. Lv, K. Wang, H. Huang, W. Zhang, S. Guo, W. Zheng, and P. Liu, Nat. Commun. **10**, 1 (2019).

[76] C. Chen, Y. Kang, Z. Huo, Z. Zhu, W. Huang, H.L. Xin, J.D. Snyder, D. Li, J.A. Herron, M. Mavrikakis, M. Chi, K.L. More, Y. Li, N.M. Markovic, G.A. Somorjai, P. Yang, and V.R. Stamenkovic, Science **343**, 1339 (2014).

[77] T.F. Jaramillo, K.P. Jørgensen, J. Bonde, J.H. Nielsen, S. Horch, and I. Chorkendorff, Science **317**, 100 (2007).

[78] A. Loiudice, P. Lobaccaro, E.A. Kamali, T. Thao, B.H. Huang, J.W. Ager, and R. Buonsanti, Angew. Chemie - Int. Ed. **55**, 5789 (2016).

[79] M.B. Gawande, A. Goswami, F.X. Felpin, T. Asefa, X. Huang, R. Silva, X. Zou, R. Zboril, and R.S. Varma, Chem. Rev. **116**, 3722 (2016).

[80] P. Loughney and V. Doan-Nguyen, in *Mater. Clean Energy Convers. Util.*, edited by L.-S. Fan

and L. Qin (ACS Books, 2020).

[81] V.R. Stamenkovic, (2014).

[82] C. Vakifahmetoglu, P. Colombo, A. Pauletti, C.F. Martin, and F. Babonneau, Int. J. Appl. Ceram. Technol. **7**, 528 (2010).

[83] C. Vakifahmetoglu, D. Zeydanli, V.C. Ozalp, B.A. Borsa, and G.D. Soraru, Mater. Des. **140**, 37 (2018).

[84] C. Vakifahmetoglu, D. Zeydanli, and P. Colombo, Mater. Sci. Eng. R Reports **106**, 1 (2016).

[85] T. Kuo, L.M. Rueschhoff, M.B. Dickerson, T.A. Patel, and K.T. Faber, Scr. Mater. **191**, 204 (2021).

[86] E.M. Susca, P.A. Beaucage, M.A. Hanson, U. Werner-Zwanziger, J.W. Zwanziger, L.A. Estroff, and U. Wiesner, Chem. Mater. **28**, 2131 (2016).

[87] D. Zeydanli, S. Akman, and C. Vakifahmetoglu, J. Am. Ceram. Soc. **101**, 2258 (2018).

[88] M.J.S. Parvulescu, K.L. Martin, P. Mogilevsky, T.A. Patel, D.P. Street, M.K. Gupta, C.S. Hung, and M.B. Dickerson, ACS Biomater. Sci. Eng. **7**, 3103 (2021).

[89] L. Schlier, N. Travitzky, J. Gegner, and P. Greil, J. Ceram. Sci. Technol. **3**, 181 (2012).

[90] C. Vakifahmetoglu, T. Semerci, and G.D. Soraru, J. Am. Ceram. Soc. **103**, 2941 (2020).

[91] P. Dibandjo, L. Bois, F. Chassagneux, D. Cornu, J.M. Letoffe, B. Toury, F. Babonneau, and P. Miele, Adv. Mater. **17**, 571 (2005).

[92] A. Choudhary, S.K. Pratihar, and S.K. Behera, RSC Adv. **6**, 95897 (2016).

[93] A. Lale, M. Schmidt, M.D. Mallmann, A.V.A. Bezerra, E.D. Acosta, R.A.F. Machado, U.B. Demirci, and S. Bernard, Surf. Coatings Technol. **350**, 569 (2018).

[94] U. Jeong, D.Y. Ryu, D.H. Kho, D.H. Lee, J.K. Kim, T.P. Russell, H. Kishi, Y. Kunimitsu, Y. Nakashima, T. Abe, J. Imade, S. Oshita, Y. Morishita, and M. Asada, Express Polym. Lett. **36**,

3626 (2015).

[95] H. Kishi, Y. Kunimitsu, Y. Nakashima, T. Abe, J. Imade, S. Oshita, Y. Morishita, and M. Asada, Express Polym. Lett. **9**, 23 (2015).

[96] J. Pan, W. Shen, Y. Zhao, H. Sun, T. Guo, Y. Cheng, N. Zhao, H. Tang, and X. Yan, Colloids Surfaces A Physicochem. Eng. Asp. **584**, 124041 (2020).

[97] M. Bernard, R. Lucas, H. Laadoua, Z. Khaldi, N. Pradeilles, O. Rapaud, S. Foucaud, R. Zerrouki, and F. Brouillette, Polym. Adv. Technol. **31**, 319 (2020).

[98] S. Packirisamy, K.J. Sreejith, D. Devapal, and B. Swaminathan, in *Handb. Adv. Ceram. Compos. Defense, Secur. Aerosp. Energy Appl.*, edited by Y. Mahajan and J. Roy (Springer International Publishing, Cham, 2020), pp. 1–107.

[99] T. Konegger, R. Patidar, and R.K. Bordia, J. Eur. Ceram. Soc. **35**, 2679 (2015).

[100] T. Konegger, L.F. Williams, and R.K. Bordia, J. Am. Ceram. Soc. **98**, 3047 (2015).

[101] K. Schelm, M. Schwidder, J. Samuel, F. Scheffler, and M. Scheffler, Adv. Eng. Mater. **19**, 1 (2017).

[102] M. Černý, Z. Chlup, A. Strachota, M. Halasová, Š. Rýglová, J. Schweigstillová, J. Svítilová, and M. Havelcová, Ceram. Int. **41**, 6237 (2015).

[103] S. Schwarz, M. Friedrich, G. Motz, and R. Kempe, Zeitschrift Fur Anorg. Und Allg. Chemie **641**, 2266 (2015).

[104] D. Schumacher, M. Wilhelm, and K. Rezwan, J. Am. Ceram. Soc. **103**, 2991 (2020).

[105] G. Glatz, T. Schmalz, T. Kraus, F. Haarmann, G. Motz, and R. Kempe, Chem. - A Eur. J. **16**, 4231 (2010).

[106] Y. Chen, J. Wei, M.S. Duyar, V. V. Ordomsky, A.Y. Khodakov, and J. Liu, Chem. Soc. Rev. **50**, 2337 (2021).

[107] Q. Zhang, J. Yu, and A. Corma, Adv. Mater. **32**, 1 (2020).

[108] V.P. Santos, T.A. Wezendonk, J.J.D. Jaén, A.I. Dugulan, M.A. Nasalevich, H.U. Islam, A. Chojecki, S. Sartipi, X. Sun, A.A. Hakeem, A.C.J. Koeken, M. Ruitenbeek, T. Davidian, G.R. Meima, G. Sankar, F. Kapteijn, M. Makkee, and J. Gascon, Nat. Commun. **6**, (2015).

[109] M. Rafati, L. Wang, and A. Shahbazi, J. CO2 Util. **12**, 34 (2015).

[110] Y. Zhang, S. Nagamori, S. Hinchiranan, T. Vitidsant, and N. Tsubaki, Energy and Fuels **20**, 417 (2006).

[111] P.K. Chauhan, R. Parameshwaran, P. Kannan, R. Madhavaram, and R. Sujith, Ceram. Int. **47**, 2591 (2021).

[112] M. Ravi and J.W. Makepeace, Chem. Sci. **13**, 890 (2022).

[113] C. Ratnasamy and J. Wagner, Catal. Rev. - Sci. Eng. **51**, 325 (2009).

[114] D. Gu, R. Ma, Y. Zhou, F. Wang, K. Yan, Q. Liu, and J. Wang, ACS Sustain. Chem. Eng. **5**, 11105 (2017).

[115] Q. Hanniet, M. Boussmen, J. Barés, V. Huon, I. Iatsunskyi, E. Coy, M. Bechelany, C. Gervais, D. Voiry, P. Miele, and C. Salameh, Sci. Rep. **10**, 1 (2020).

[116] A. Saha, S.R. Shah, R. Raj, and S.E. Russek, J. Mater. Res. **18**, 2549 (2003).

[117] N. Yang and K. Lu, Carbon N. Y. **171**, 88 (2021).

[118] J.K. Nørskov, F. Studt, F. Abild-Pedersen, and T. Bligaard, 97 (2014).

[119] C. Vakifahmetoglu, E. Pippel, J. Woltersdorf, and P. Colombo, J. Am. Ceram. Soc. **93**, 959 (2010).

[120] C. Vakifahmetoglu, P. Colombo, S.M. Carturan, E. Pippel, and J. Woltersdorf, J. Am. Ceram. Soc. **93**, 3709 (2010).

[121] M. Zaheer, G. Motz, and R. Kempe, J. Mater. Chem. **21**, 18825 (2011).

[122] M. Zaheer, J. Hermannsdörfer, W.P. Kretschmer, G. Motz, and R. Kempe, ChemCatChem **6**, 91 (2014).

[123] M. Zaheer, C.D. Keenan, J. Hermannsdörfer, E. Roessler, G. Motz, J. Senker, and R. Kempe, Chem. Mater. **24**, 3952 (2012).

[124] H.P. Macedo, R.L.B.A. Medeiros, J. Ilsemann, D.M.A. Melo, K. Rezwan, and M. Wilhelm, Microporous Mesoporous Mater. **278**, 156 (2019).

[125] M. Zaheer, T. Schmalz, G. Motz, and R. Kempe, Chem. Soc. Rev. **41**, 5102 (2012).

[126] C. Zhou, C. Fasel, R. Ishikawa, M. Gallei, Y. Ikuhara, S. Lauterbach, H.J. Kleebe, R. Riedel, and E. Ionescu, J. Eur. Ceram. Soc. **37**, 5193 (2017).

[127] A.M. Wilson, J.N. Reimers, E.W. Fuller, and J.R. Dahn, Solid State Ionics **74**, 249 (1994).

[128] W. Xing, A.M. Wilson, K. Eguchi, G. Zank, and J.R. Dahn, J. Electrochem. Soc. **144**, 2410 (1997).

[129] H. Fukui, H. Ohsuka, T. Hino, and K. Kanamura, ACS Appl. Mater. Interfaces **2**, 999 (2010).

[130] M. Graczyk-Zajac, L.M. Reinold, J. Kaspar, P.V.W. Sasikumar, G.D. Soraru, and R. Riedel, Nanomaterials **5**, 233 (2014).

[131] J. Shen and R. Raj, J. Power Sources **196**, 5945 (2011).

[132] F. Toigo, Additive Manufacturing of SiOC Composites and Investigation of Their Electrochemical Behaviour for Energy Storage Application, 2019.

[133] S. Bin Mujib, R. Cuccato, S. Mukherjee, G. Franchin, P. Colombo, and G. Singh, Ceram. Int. **46**, 3565 (2020).

[134] J.R. Dahn, T. Zheng, Y. Liu, and J.S. Xue, Science **270**, 590 (1995).

[135] J. Saint, M. Morcrette, D. Larcher, L. Laffont, S. Beattie, J.P. Pérès, D. Talaga, M. Couzi, and J.M. Tarascon, Adv. Funct. Mater. **17**, 1765 (2007).

[136] J. Wang, S. Li, Y. Zhao, J. Shi, L. Lv, H. Wang, Z. Zhang, and W. Feng, RSC Adv. **8**, 6660 (2018).

[137] A.M. Wilson and J.R. Dahn, J. Electrochem. Soc. **142**, 326 (1995).

[138] J.W. Kim, J.H. Ryu, K.T. Lee, and S.M. Oh, J. Power Sources **147**, 227 (2005).

[139] J.S. Xue, K. Myrtle, and J.R. Dahn, J. Electrochem. Soc. **142**, 2927 (1995).

[140] P. Dibandjo, M. Graczyk-Zajac, R. Riedel, V.S. Pradeep, and G.D. Soraru, J. Eur. Ceram. Soc. **32**, 2495 (2012).

[141] J. Kaspar, M. Graczyk-Zajac, and R. Riedel, Solid State Ionics **225**, 527 (2012).

[142] J. Kaspar, M. Graczyk-Zajac, and R. Riedel, J. Power Sources **244**, 450 (2013).

[143] D. Ahn and R. Raj, J. Power Sources **195**, 3900 (2010).

[144] J. Kaspar, M. Graczyk-Zajac, S. Choudhury, and R. Riedel, Electrochim. Acta **216**, 196 (2016).

[145] H. Sun and K. Zhao, ACS Appl. Mater. Interfaces **9**, 35001 (2017).

[146] V. Liebau-Kunzmann, C. Fasel, R. Kolb, and R. Riedel, J. Eur. Ceram. Soc. **26**, 3897 (2006).

[147] D. Su, Y.L. Li, Y. Feng, and J. Jin, J. Am. Ceram. Soc. **92**, 2962 (2009).

[148] M. Graczyk-Zajac, G. Mera, J. Kaspar, and R. Riedel, J. Eur. Ceram. Soc. **30**, 3235 (2010).

[149] G. Liu, J. Kaspar, L.M. Reinold, M. Graczyk-Zajac, and R. Riedel, Electrochim. Acta **106**, 101 (2013).

[150] Y. Feng, S. Dou, Y. Wei, Y. Zhang, X. Song, X. Li, and V.S. Battaglia, ACS Omega **2**, 8075 (2017).

[151] S. Mukherjee, Z. Ren, and G. Singh, J. Phys. D. Appl. Phys. **51**, (2018).

[152] H. Konno, T. Morishita, S. Sato, H. Habazaki, and M. Inagaki, Carbon N. Y. **43**, 1111 (2005).

[153] Z. Wu, X. Cheng, D. Tian, T. Gao, W. He, and C. Yang, Chem. Eng. J. **375**, (2019).

[154] Y. Feng, G.X. Du, X.J. Zhao, and E.C. Yang, J. Appl. Electrochem. **41**, 999 (2011).

[155] L. David, D. Asok, and G. Singh, ACS Appl. Mater. Interfaces **6**, 16056 (2014).

[156] H. Huang, C. Shi, R. Fang, Y. Xia, C. Liang, Y. Gan, J. Zhang, X. Tao, and W. Zhang, Chem. Eng. J. **359**, 584 (2019).

[157] M. Idrees, S. Batool, J. Kong, Q. Zhuang, H. Liu, Q. Shao, N. Lu, Y. Feng, E.K. Wujcik, Q. Gao, T. Ding, R. Wei, and Z. Guo, Electrochim. Acta **296**, 925 (2019).

[158] S. Mukherjee, S. Bin Mujib, D. Soares, and G. Singh, Materials (Basel). **12**, (2019).

[159] J. Kaspar, M. Storch, C. Schitco, R. Riedel, and M. Graczyk-Zajac, J. Electrochem. Soc. **163**, A156 (2016).

[160] Y. Lee, K.Y. Lee, and W. Choi, Adv. Funct. Mater. **27**, 1 (2017).

[161] C. Chandra and J. Kim, Chem. Eng. J. **338**, 126 (2018).

[162] D.M. Soares and G. Singh, Nanotechnology **31**, (2020).

[163] R.N. Putra, M. Halim, G. Ali, S.F. Shaikh, A.M. Al-Enizi, T. Fazal, F. Jan Iftikhar, and A.N.S. Saqib, New J. Chem. **44**, 14035 (2020).

[164] B. Dong, Y. Han, T. Wang, Z. Lei, Y. Chen, F. Wang, H. Abadikhah, S.A. Khan, L. Hao, X. Xu, R. Cao, L. Yin, and S. Agathopoulos, ACS Appl. Energy Mater. **3**, 10183 (2020).

[165] V.S. Pradeep, D.G. Ayana, M. Graczyk-Zajac, G.D. Soraru, and R. Riedel, Electrochim. Acta **157**, 41 (2015).

[166] Z. Zhang, J.E. Calderon, S. Fahad, L. Ju, D.X. Antony, Y. Yang, A. Kushima, and L. Zhai, ACS Appl. Mater. Interfaces **13**, 9794 (2021).

[167] J. Shen, D. Ahn, and R. Raj, J. Power Sources **196**, 2875 (2011).

[168] R. Bhandavat and G. Singh, ACS Appl. Mater. Interfaces **4**, 5092 (2012).

[169] L. David, S. Bernard, C. Gervais, P. Miele, and G. Singh, J. Phys. Chem. C **119**, 2783 (2015).

[170] S.K. Behera and R. Raj, Chem. Commun. **49**, 9657 (2013).

[171] D. Kim, H. Kim, H. Lim, K.J. Kim, H.G. Jung, D. Byun, C. Kim, and W. Choi, Int. J. Energy Res. **44**, 11473 (2020).

[172] K. Wang, B. Ma, X. Li, Y. Wang, and L. An, J. Phys. Chem. A **119**, 552 (2015).

[173] G.D. Soraru and L. Pederiva, J. Am. Ceram. Soc. **85**, 2181 (2002).

[174] E. Bernardo, L. Fiocco, G. Parcianello, E. Storti, and P. Colombo, Materials (Basel). **7**, 1927 (2014).

[175] T.S. Key, G.B. Wilks, and M.K. Cinibulk, J. Am. Ceram. Soc. **Accepted A**, 1 (2021).

[176] N. Yang and K. Lu, J. Am. Ceram. Soc. 1 (2021).

[177] S.A. Khan, S.B. Khan, L.U. Khan, A. Farooq, K. Akhtar, and A.M. Asiri, in *Handb. Mater. Charact.*, edited by S.K. Sharma (Springer International Publishing, 2018), pp. 317–344.

[178] S.J. Widgeon, S. Sen, G. Mera, E. Ionescu, R. Riedel, and A. Navrotsky, Chem. Mater. **22**, 6221 (2010).

[179] I. Hung, E. Ionescu, J. Sen, Z. Gan, and S. Sen, J. Phys. Chem. C **125**, 4777 (2021).

[180] B.D. Cullity and S.R. Stock, *Elements of X-Ray Diffraction*, Third (Pearson, Harlow, Essex, 2014).

[181] O. Glatter and O. Kratky, *Small Angle X-Ray Scattering* (Academic Press, Inc., New York, 1982).

[182] A. Guinier and G. Fournet, *Small-Angle Scattering of X-Rays* (John Wiley & Sons, New York, N.Y., 1955).

[183] T. Egami and S.J.L. Billinge, *Underneath the Bragg Peaks: Structural Analysis of Complex Materials*, 2nd ed. (Elsevier, Amsterdam, 2003).

[184] D.B. Williams and C.B. Carter, *Transmission Electron Microscopy, Part 1: Basics* (1996).

[185] A.J. Chancellor, B.T. Seymour, and B. Zhao, Anal. Chem. (2019).

[186] P.F. Green, Soft Matter **7**, 7914 (2011).

[187] T.B. Martin, K.I.S. Mongcopa, R. Ashkar, P. Butler, R. Krishnamoorti, and A. Jayaraman, J. Am. Chem. Soc. **137**, 10624 (2015).

[188] E. Ionescu, C. Terzioglu, C. Linck, J. Kaspar, A. Navrotsky, and R. Riedel, J. Am. Ceram. Soc. **96**, 1899 (2013).

[189] M.W. Terban, A.M. Pütz, G. Savasci, U. Heinemeyer, B. Hinrichsen, P. Desbois, and R.E. Dinnebier, J. Polym. Sci. **58**, 1843 (2020).

[190] M. Zobel, R.B. Neder, and S.A.J. Kimber, Science **347**, 292 (2015).

[191] T. Konegger, C. Drechsel, and H. Peterlik, Microporous Mesoporous Mater. **324**, 111268 (2021).

[192] R.T. Bell, P.A. Beaucage, M.J. Murphy, A.B. Connolly, U. Wiesner, D. Ginley, R.B. Van Dover, and M.O. Thompson, Chem. Mater. **33**, 4328 (2021).

[193] C. Ophus, Microsc. Microanal. 563 (2019).

[194] N. Yang, C. Ophus, B.H. Savitzky, M.C. Scott, K. Bustillo, and K. Lu, Mater. Charact. **181**, 111512 (2021).

[195] G. Gourdin and V. Doan-Nguyen, Cell Reports Phys. Sci. **2**, 1 (2021).

FIG. 1. Flexible polymer-derived ceramic processing enables tunability of functionalities and properties starting from molecular design. Scheme depicts crosslinking and pyrolysis of generic silicon-based preceramic polymer in which blue atoms represent Si, red E atoms are O or N-R_3 (R_1, R_2, R_3 = H, CH, -CH=CH_2, C_6H_5, etc), and gray atoms represent C.

FIG. 2. (a) DC conductivity as a function of temperature for the 0.05 wt% Ti_3C_2-SiOC samples. Each data point is the average of three measurements, and (b) *log (σ(T))* as a function of $T^{-0.25}$ between room temperature and 400°C, showing a linear relationship.

FIG. 3. Frequency dependence of the real and imaginary impedances for flash pyrolyzed SiC-TiC samples. The Ti to Si molar ratio is: (a) 0, (b) 0.05, (c) 0.10, and (d) 0.20.[60] (Reproduced with permission from Journal of the American Ceramic Society 104, 2460 (2021).[60] Copyright 2021 John Wiley and Sons.)

FIG. 4. (a) Complex impedance spectra of 0.05 wt% Ti_3C_2-SiOC as a function of measurement temperature, (b) Nyquist plot of the room temperature complex impedance spectra of 0.05 wt% Ti_3C_2-SiOC along with simulated circuit results (dash line) and their corresponding electrical circuit diagrams.

FIG. 5. Frequency dependence of the (a) real impedance and (b) imaginary impedance of 0.05 wt% Ti_3C_2-SiOC.

FIG. 6. Magnetic hysteresis loops in Ni-SiOC ceramics pyrolyzed at different temperatures: a) 800^0 C, b) 900^0C, and c) 1100^0C. Reproduced with permission from *Journal of the American Ceramic Society* 103, 145 (2020).[61] Copyright 2020 John Wiley and Sons.)

FIG. 7. (a) Magnetization M versus applied field H for SiFeOC ceramic samples obtained upon pyrolysis of polymethylsilsesquioxane modified with 50 wt% $Fe(acac)_3$ at different pyrolysis temperatures. (b) Magnetization M versus applied field H for SiFeOC ceramic samples prepared with 5 wt% and 15 wt% $Fe(acac)_3$ at 1100^0C and 1400^0C, respectively. Reproduced with permission from *Journal of the European Ceramic Society* 33, 2465 (2013).[72] Copyright 2013 Elsevier.)

FIG. 8. Schematic of PDCs that could be designed to contain graded, hierarchical porosity with a range of (a) uniform or (b) graded micropores (white) connecting biomorphic cellular structures consisting of mesopores for enhanced gas flow kinetics. Rendering significantly modified from Choudhary and co-workers[92]. Reproduced with permission from RSC Advances 6, 95897 (2016). Copyright 2016 Royal Society of Chemistry.

FIG. 9. The most common precursors used for synthesis of polymer-derived (a) SiOC and (b) SiCN and their microstructures. Schematic representation of SiOC and SiCN as active electrode materials in EESS. The green Li^+/Na^+ ions stored reversibly in the systems, whereas gray Li/Na ions are captured irreversibly. The phase diagram of (c) SiOC and (d) SiCN ternary systems. The high capacity occurs towards the green shaded area in the center of the pyramids.

AIP Publishing

Journal of Applied Physics

ACCEPTED MANUSCRIPT

This is the author's peer reviewed, accepted manuscript. However, the online version of record will be different from this version once it has been copyedited and typeset.
PLEASE CITE THIS ARTICLE AS DOI: 10.1063/5.0085844

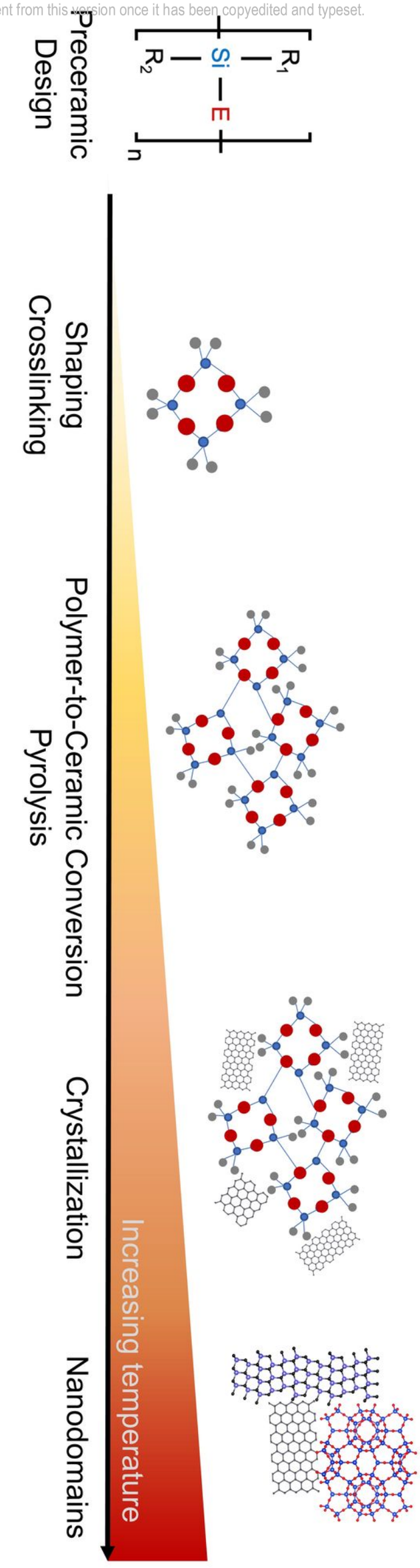

Figure 2

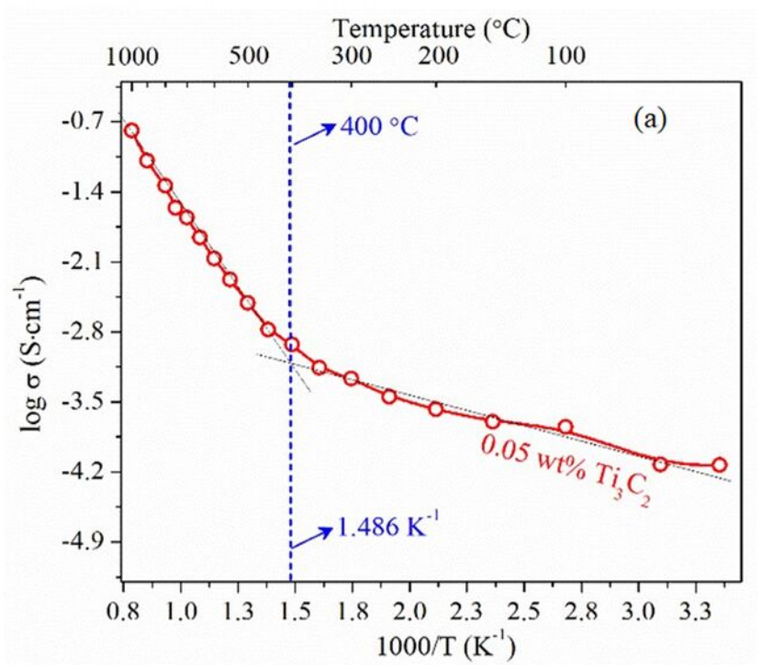

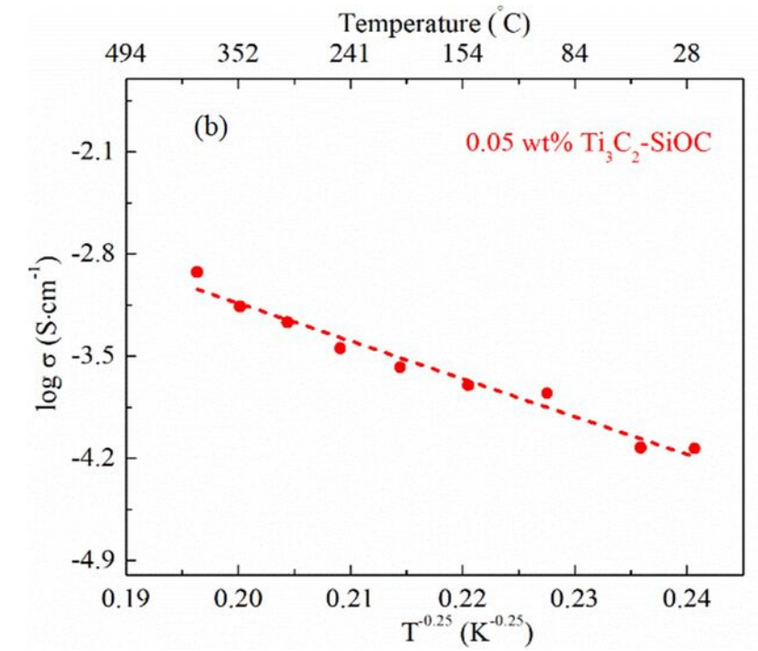

AIP Publishing

Journal of Applied Physics

ACCEPTED MANUSCRIPT

PLEASE CITE THIS ARTICLE AS DOI: 10.1063/5.0085844

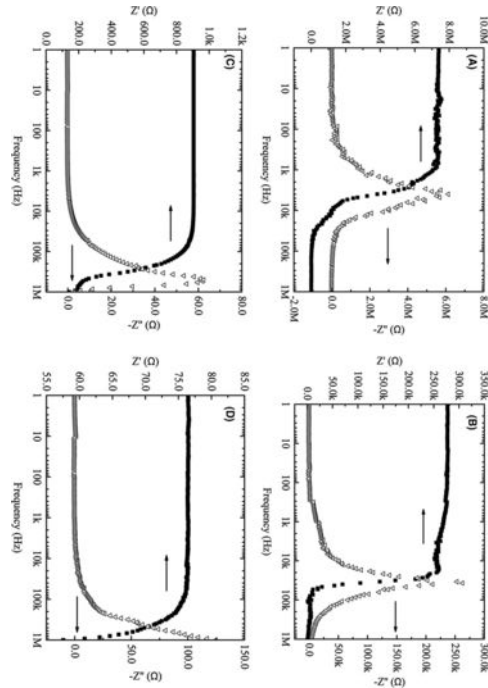

AIP Publishing

Journal of Applied Physics

ACCEPTED MANUSCRIPT

This is the author's peer reviewed, accepted manuscript. However, the online version of record will be different from this version once it has been copyedited and typeset.
PLEASE CITE THIS ARTICLE AS DOI: 10.1063/5.0085844

Figure 4

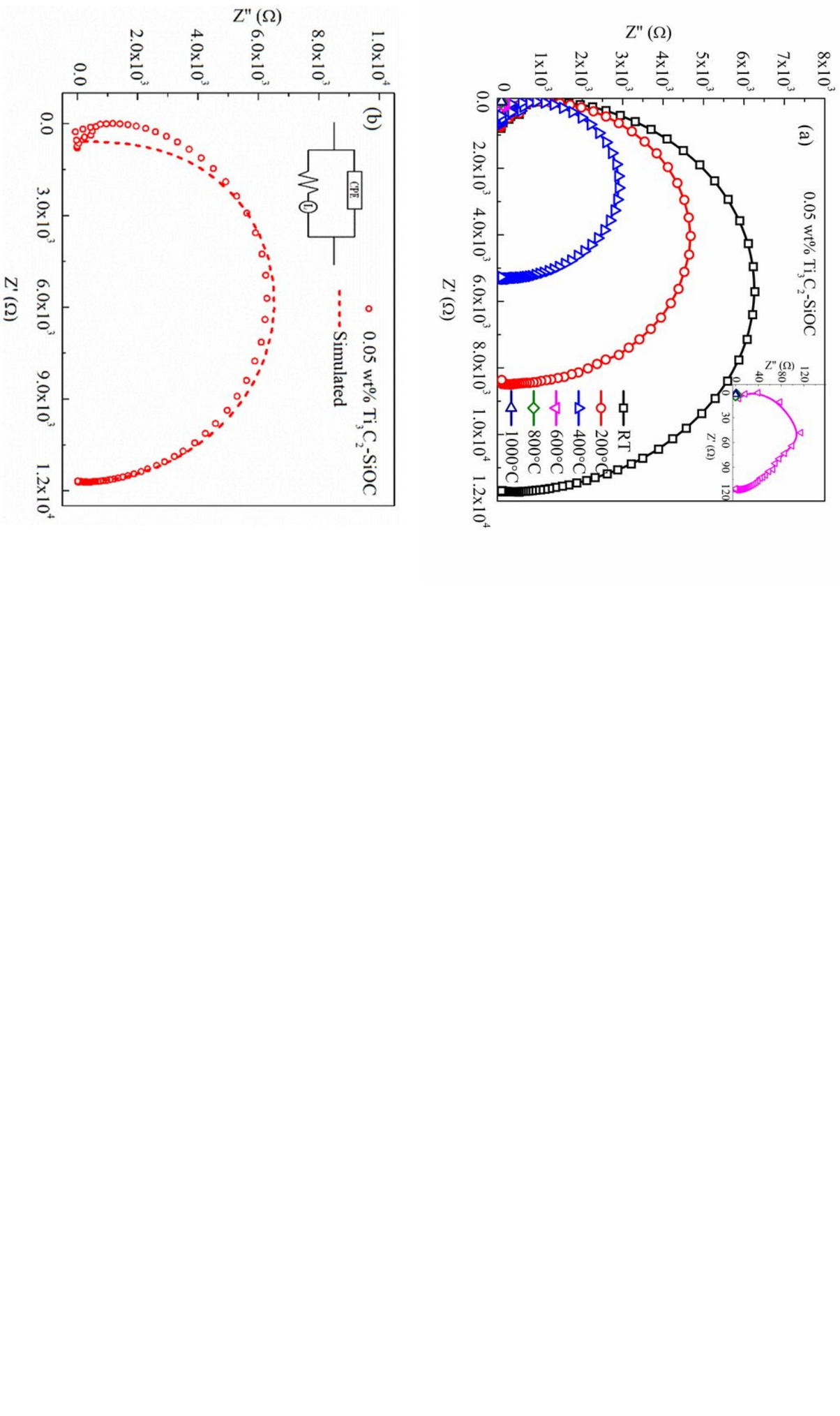

Figure 5

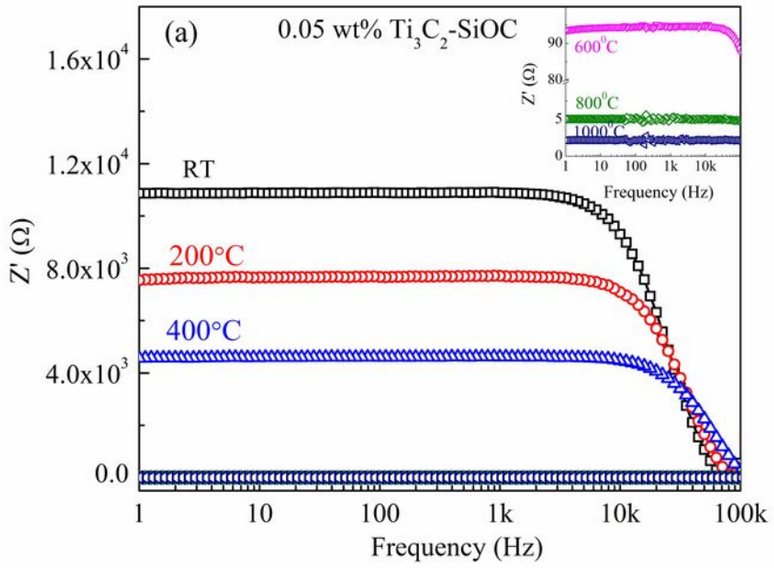

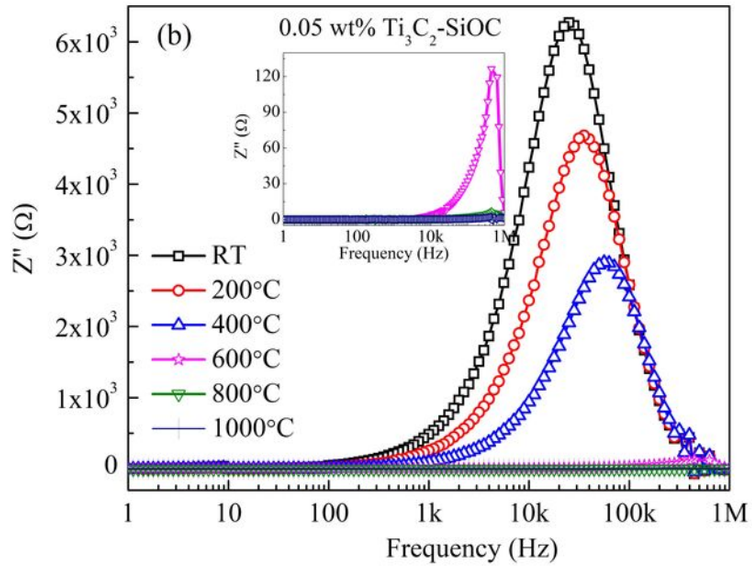

Journal of Applied Physics

Figure 6

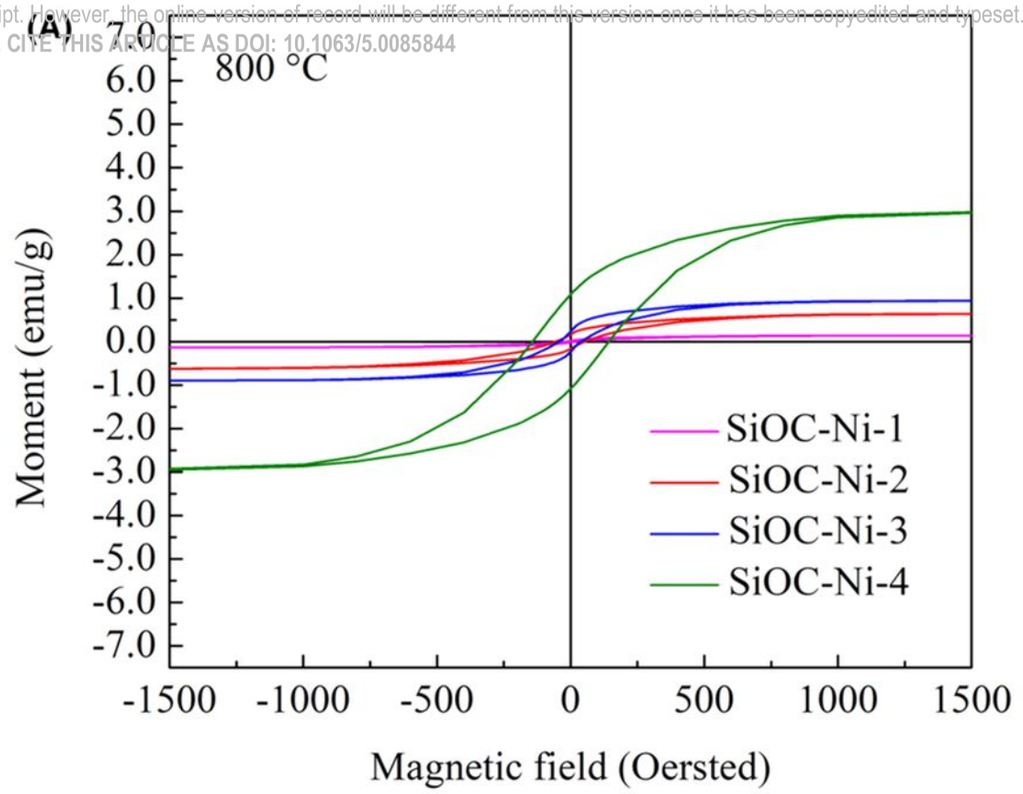

AIP Publishing

Journal of Applied Physics

ACCEPTED MANUSCRIPT

This is the author's peer reviewed, accepted manuscript. However, the online version of record will be different from this version once it has been copyedited and typeset.
PLEASE CITE THIS ARTICLE AS DOI: 10.1063/5.0085844

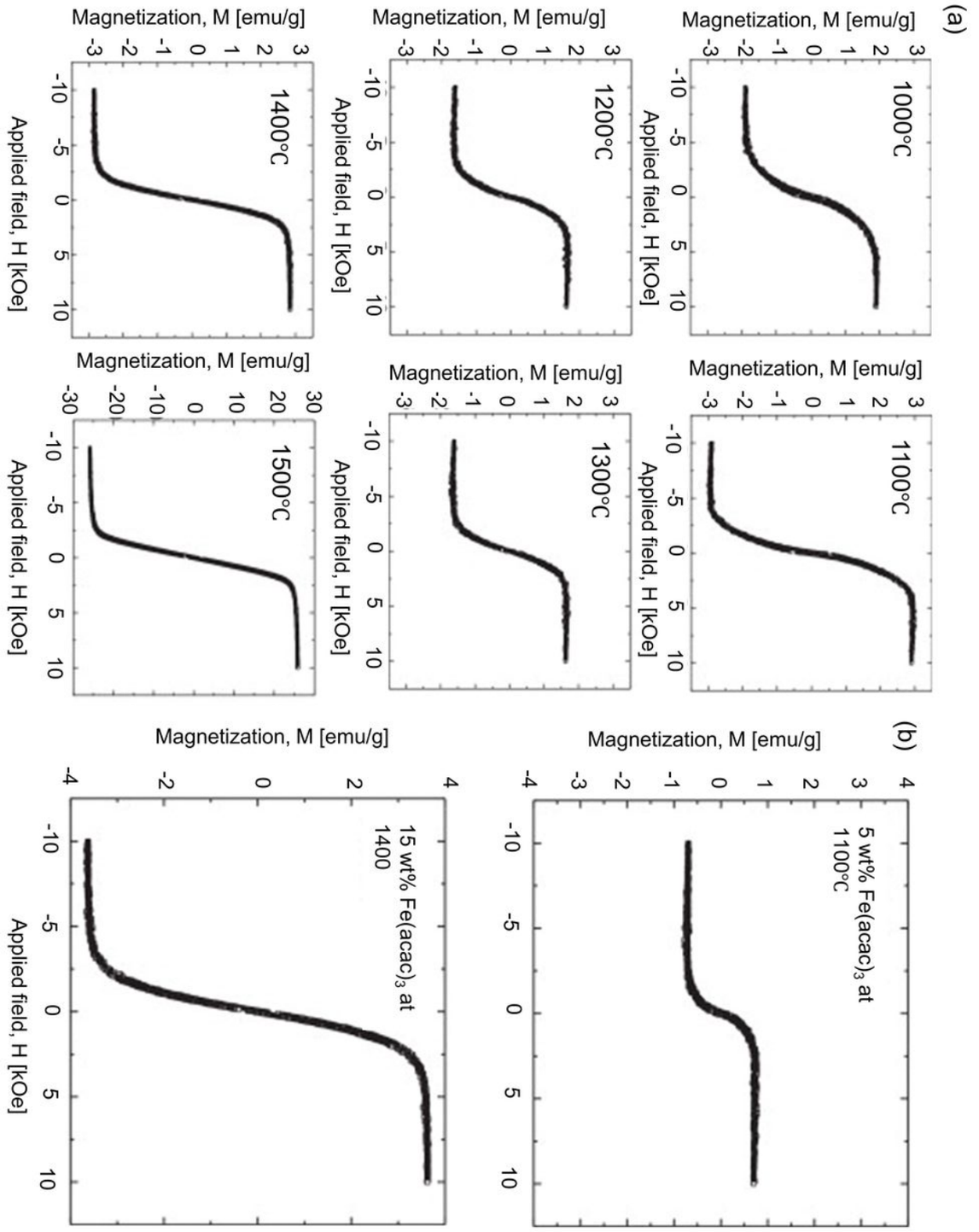

AIP Publishing

Journal of Applied Physics

ACCEPTED MANUSCRIPT

PLEASE CITE THIS ARTICLE AS DOI: 10.1063/5.0085844

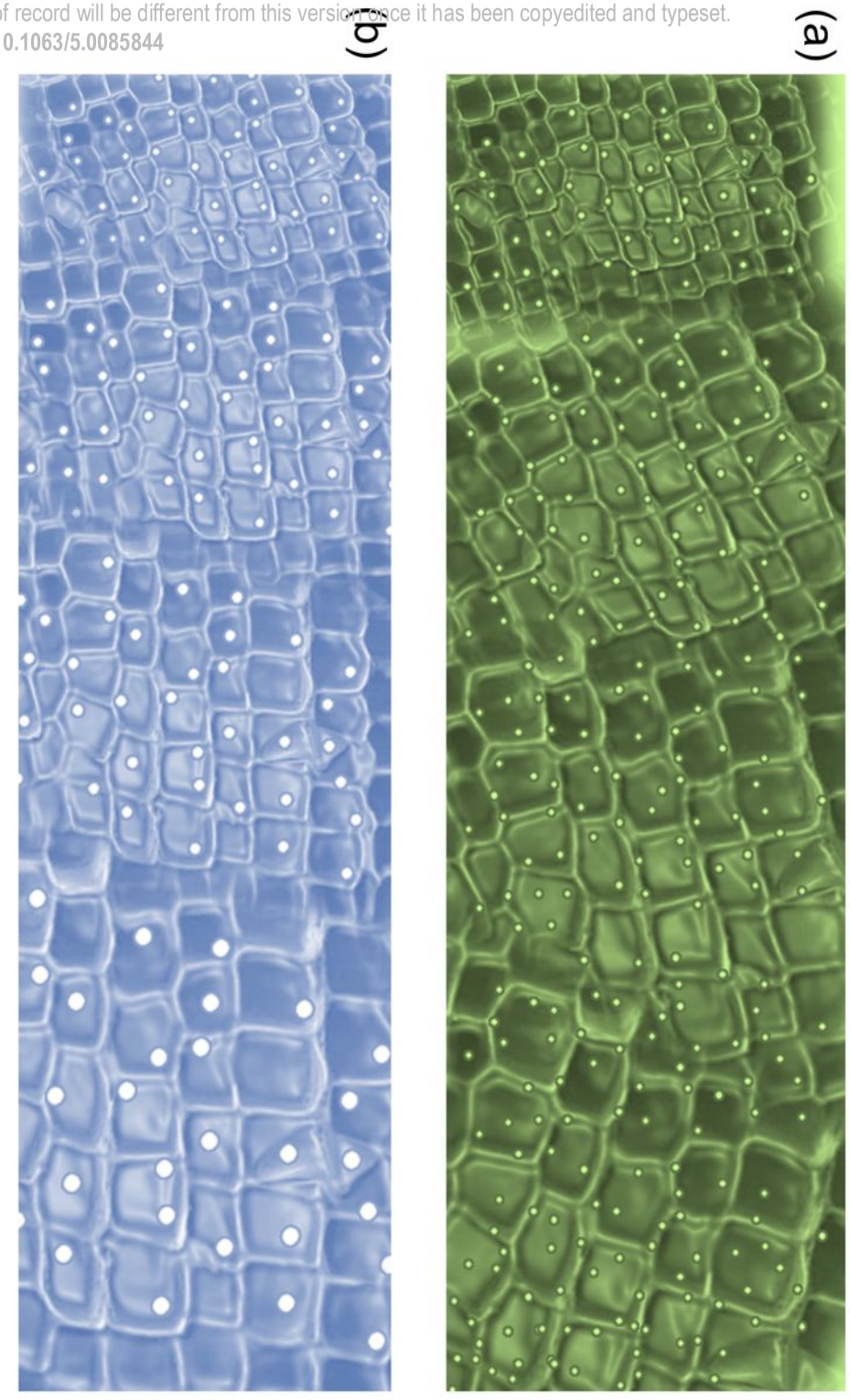

Journal of Applied Physics